Technical University of Denmark

DTU

Crystalline electrical fields in dilute rare earths studied by neutron scattering

Rathmann, Ole Steen

Publication date:
1976

Document Version
Publisher's PDF, also known as Version of record

Link back to DTU Orbit

Citation (APA):
Rathmann, O. (1976). Crystalline electrical fields in dilute rare earths studied by neutron scattering. (Denmark. Forskningscenter Risoe. Risoe-R; No. 337).

DTU Library
Technical Information Center of Denmark

Risø Report No. 337

Research Establishment Risø

Crystalline Electrical Fields in Dilute Rare Earths Studied by Neutron Scattering

by O. Rathmann

March 1976

Crystalline Electrical Fields in Dilute Rare Earths
Studied by Neutron Scattering

by

O. Rathmann

Danish Atomic Energy Commission
Research Establishment Risø
Physics Department

Abstract

The spectra of the crystalline electrical field excitations were measured in the dilute rare earth alloys Y-1% Dy, Y-2% Er, Sc-2% Er and Lu-2% Er by means of inelastic neutron scattering. The results agree with earlier published papers reporting magnetization measurements on the same kinds of alloy, when an improved method of analysis, which takes ordering effects into account, is applied to the magnetization data.

In contrast to the first conclusion of these earlier papers, the present limited results suggest that the fourth- and sixth--order components of the crystalline electrical field $(B_{40}/\beta,$ B_{60}/γ and $B_{66}/\gamma)$ are almost independent of both rare earth and diluent whereas (B_{20}/α) depends on the diluent.

CONTENTS

1. INTRODUCTION

The rare earth metals are perhaps the most exciting of the magnetic elements. The paramagnetism observed in the pure metals, as well as in their alloys, is highly anisotropic, and exotically ordered magnetic structures appear at low temperature.

The main aim of this study was, by means of inelastic neutron scattering, to investigate the so-called Crystalline Electrical Field (CEF) of dilute rare earth alloys because the CEF is the dominant source of the anisotropy. This study was motivated by systematic magnetization measurements by Høg and Touborg on heavy rare earths diluted in non-magnetic matrices[1]. These measurements seemed to indicate that, in contrast to the predictions of the simple external charge model (see chapter 2), the rare earth itself was the decisive factor for the CEF.

In close contact with P. Touborg and in the light of the magnetization results, the CEF was therefore deduced from the completely different spectroscopic method of inelastic neutron scattering.

In connection with these measurements some neutron diffraction studies of ordered magnetic structures were additionally performed.

The main results were described in two papers[2,3]; thus chapters 4 and 5, describing the measurements and the analysis, serve to gather together all results, making reference to the two papers where possible.

All the neutron scattering experiments were performed on triple-axis spectrometers at the DR 3 reactor at Risø.

2. RARE EARTH MAGNETISM

Rare earth magnetism is caused by the unfilled 4f electron shell[4], which is quite analogous to the unfilled 3d shell in the iron group. However, because it is well placed inside the filled $5s^2p^6$-shell, the 4f shell of a rare earth ion (with few exceptions the rare earths appear as tripositive ions in metals) is far better screened and localized than a 3d-shell in an iron-group ion. Quantitatively this means that, at least for the heavy rare earths, the interaction of a 4f shell with its surroundings, a

few hundred K in size, is smaller than the spin-orbit coupling
of several thousand K (see Δ_o in table 2.1) that is the smallest
interaction inside a shell.

So, besides the quantum numbers for the total spin, S, and
for the orbital angular momentum, L, the quantum number for the
total angular momentum $J(J = L + S)$ remains a good quantum number.
In table 2.1 these quantum numbers are given for the heavy rare
earth ions.
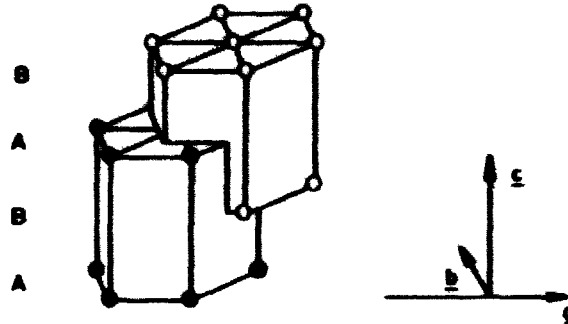
Fig. 2.1. Hexagonal, close-packed (hcp) structure. The structure
consists of hexagonal layers stacked in the sequence ABAB ......
The B-layers look exactly like the A-layers but are transposed
($\frac{2}{3}$ a + $\frac{1}{3}$ b + $\frac{1}{2}$ c) with respect to these. The heavy rare earths
have c/a ratios about 4% lower than the ideal hcp value $\sqrt{\frac{8}{3}}$.

At and below room temperature all heavy rare earth metals,
except Yb, appear in the hcp structure, shown on fig. 2.1. Although
the local symmetry is trigonal, the 4f shell senses a hexagonal
"effective" symmetry.

The Coulomb interaction between a 4f shell and the surroundings,
which produces the magnetic properties, falls naturally into three
contributions:
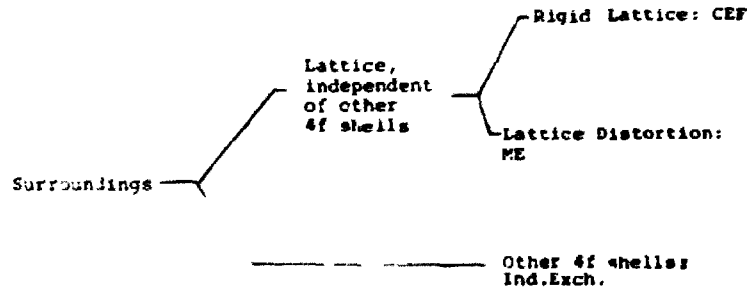
$H_{4f} = H_{EXCH} + H_{CEF} + H_{ME}$

CEF: Crystalline Electrical Field
ME: Magneto Elastic Interaction
Ind. Exch.: Indirect exchange

Table 2.1

Quantum numbers and other electronic properties of the heavy tripositive rare earth ions[4]

J^{3+} ion	Gd	Tb	Dy	Ho	Er	Tm	Yb	Lu
N_{4f}	7	8	9	10	11	12	13	14
L	0	3	5	6	6	5	3	0
S	$\frac{7}{2}$	3	$\frac{5}{2}$	2	$\frac{3}{2}$	1	$\frac{1}{2}$	0
J	$\frac{7}{2}$	6	$\frac{15}{2}$	8	$\frac{15}{2}$	6	$\frac{7}{2}$	0
g	2	$\frac{3}{2}$	$\frac{4}{3}$	$\frac{5}{4}$	$\frac{6}{5}$	$\frac{7}{6}$	$\frac{8}{7}$	0
$(g-1)^2(J+1)J$	15.75	10.5	7.08	4.50	2.55	1.17	0.32	0
Δ_0 (K)	-	2900	4700	7500	9400	11900	14800	
$\alpha_2 \cdot 10^3 = \alpha \cdot 10^3$	-	-10.1	-6.35	-2.22	2.54	10.1	31.7	
$\alpha_4 \cdot 10^5 = \beta \cdot 10^5$	-	12.2	-5.92	-3.33	4.44	16.3	-173	
$\alpha_6 \cdot 10^6 = \gamma \cdot 10^6$	-	-1.12	1.03	-1.30	2.07	-5.60	148	

$g = \frac{3}{2} + \frac{S(S+1) + L(L+1)}{2J(J+1)}$ is the Lande splitting factor, and

Δ_0 is the approximate splitting up to the first excited J-multiplet.

α_2, α_4 and α_6 are Stevens factors defined in eq. (2.1a).

2.1. Dilute Rare Earths

If a rare earth is sufficiently diluted by substitution in a non-magnetic host metal, the exchange interaction between the rare earth ions may be made negligibly small. In order to keep the CEF-interaction as close as possible to that of the pure rare earths, the non-magnetic diluent must have 1) a crystal structure nearly identical to that of the pure rare earths, and 2) the same outer electronic structure as the pure rare earths.

As seen in table 2.2, the non-magnetic metals Sc, Y and Lu are good candidates for such diluents[5].

- 8 -

Table 2.2

Crystallographic and electronic properties of rare earths and possible diluents.

	Crystal structure (hcp)			Electronic structure
	a(Å)	c(Å)	c/a	
Sc	3.309	5.273	1.594	(Ar) $3d\ 4s^2$
Y	3.650	5.741	1.5750	(Kr) $4d\ 5s^2$
Lu	3.510	5.567	1.5797	(Kr) $4d^{10}\ 4f^{14}\ 5s^2p^6\ \underline{5d\ 6s^2}$
Tb	3.601	5.694	1.5811	(Kr) $4d^{10}\ 4f^8\ \underline{4f}\ 5s^2p^6\ \underline{6s^2}$
Dy	3.593	5.654	1.5735	(Kr) $4d^{10}\ 4f^9\ \underline{4f}\ 5s^2p^6\ \underline{6s^2}$
Er	3.561	5.593	1.5706	(Kr) $4d^{10}\ 4f^{11}\ \underline{4f}\ 5s^2p^6\ \underline{6s^2}$

The underlined part of the outer electronic configuration forms the conduction band.

The ideal hcp structure has a c/a = $\sqrt{\frac{8}{3}}$ = 1.6330

2.2. Crystalline Electrical Field

Disregarding the interaction between 4f spins for a moment, the simple picture of the origin of the CEF is this: The neighbouring ions around a given rare earth ion form a highly inhomogeneous charge distribution producing a non-uniform electrical field at the place of the 4f-shell.

As the unfilled 4f-shell is non-spherical, it will have preferred orientations in this field and consequently the 4f spin will have preferred directions.

For the rare earth hcp-metals this CEF may be described by 4 parameters. With the standard choice of coordinate system (x-axis along a and z-axis along c), the crystal field acting on the 4f electrons may be multipole expanded from the centre of the 4f-shell[6]:

$$V(\underline{r}) = \sum_{L=0}^{\infty} \sum_{M=0}^{L} A_{LM} P_{LM}(x,y,z).$$ (2.1)

The homogeneous polynomials P_{LM} (with integer coefficients) correspond to the spherical harmonics $r^L\ Y_{LM}(\phi,\theta)$ and the most important are given in table 2.3.

According to the Wigner-Eckart theorem, we may express $V(r)$ in terms of the more suitable angular momentum variables by using the equivalence

$$P_{LM}(x,y,z) \sim \langle r^L \rangle \; \alpha_L \; \hat{O}_{LM}(\hat{\underline{J}}). \qquad (2.1a)$$

Here the equivalence sign $\sim$ means that the two operators have equal matrix elements between states of a 4f-shell with fixed J.

The most important of the Stevens operators $\hat{O}_{LM}(\hat{J})$ are given in table 2.3, while the Stevens factors α_L, depending on the rare earth, are listed in table 2.1. $\langle r^L \rangle$ is the L'th moment of the 4f radius decreasing somewhat through the series of tripositive rare earth ions[7]. Two arguments limit the number of terms needed in the multipole expansion. The 4f-electrons (l=3) are insensitive to multipole components with L odd or with L > 6, and of the rest only 4 are consistent with the hcp symmetry. Using $B_{LM} = \langle r^L \rangle \; \alpha_L \; A_{LM}$ the CEF-Hamiltonian thus reads

$$H_{CEF} = B_{20} \hat{O}_{20} + B_{40} \hat{O}_{40} + B_{60} \hat{O}_{60} + B_{66} \hat{O}_{66}. \qquad (2.2)$$

For ideal hcp structure with only nearest-neighbour interaction, there are further simplifications[5]:

$$A_{20} = 0 \qquad (2.3)$$

$$A_{66} = - \frac{77}{8} A_{60} . \qquad (2.4)$$

$A_{20} = 0$ may be understood from a very simple argument. The local symmetry of an ion in an ideal hcp-structure (see fig. 2.1) may be changed to that of a fcc (face centered cubic) structure just by rotating one of the neighbouring hexagonal planes through 180° about the hexagonal axis which passes through the regarded ion. Now A_{20} only describes an axial anisotropy, singling out a particular crystallographic axis and is thus unchanged by this rotation. However, in the cubic fcc structure no single preferred direction exists and thus $A_{20} = 0$. The relation between A_{66} and A_{60} may be derived in a similar way.

For non ideal hcp structures one may use a nearest neighbour point charge model to show that A_{20} depends on the c/a ratio, approximately in proportion to

$$\left\{ 1 - \left[(c/a)/(c/a)_{ideal} \right]^2 \right\} \ .$$

Table 2.3

Some homogeneous polynomials P_k^q of even degree, frequently used in multiple expansions of CEF, together with their equivalent Stevens operators $\hat{O}_k^q(J)$. The notation $(A\ B)_s$ is used as shorthand for $\frac{1}{2}(AB + BA)$. From[6].

$$P_2^0 = 3z^2 - r^2 \qquad\qquad P_2^2 = x^2 - y^2$$

$$P_4^0 = 35z^4 - 30r^2z^2 - 3r^4 \qquad P_4^2 = (7z^2 - r^2)(x^2 - y^2)$$

$$P_4^3 = xz(x^2 - 3y^2) \qquad\qquad P_4^4 = x^4 - 6x^2y^2 + y^4$$

$$P_6^0 = 231z^6 - 315r^2z^4 + 105r^4z^2 - 5r^6 \qquad P_6^2 = (11z^2 - 3r^2)(x^2 - 3y^2)xz$$

$$P_6^3 = (11z^2 - r^2)(x^4 - 6x^2y^2 - y^4) \qquad P_6^4 = x^6 - 15x^4y^2 - 15x^2y^4 - y^6$$

$$k = 2 \quad \begin{cases} O_2^0 = 3J_z^2 - J(J+1) \\ O_2^2 = \frac{1}{2}(J_+^2 - J_-^2) \end{cases}$$

$$k = 4 \quad \begin{cases} O_4^0 = 35J_z^4 - 30J(J+1)J_z^2 - 25J_z^2 - 6J(J+1) - 3J^2(J+1)^2 \\ O_4^2 = \frac{1}{2}\{(7J_z^2 - J(J+1) - 5)(J_+^2 - J_-^2)\}_s \\ O_4^3 = \frac{1}{2}\{J_z(J_+^2 - J_-^2)\}_s \\ O_4^4 = \frac{1}{2}(J_+^4 - J_-^4) \end{cases}$$

$$k = 6 \quad \begin{cases} O_6^0 = 231J_z^6 - 315J(J+1)J_z^4 + 735J_z^4 - 105J^2(J+1)^2J_z^2 + 525J(J+1)J_z^2 \\ \qquad\quad - 294J_z^2 - 5J^3(J+1)^3 + 40J^2(J+1)^2 - 60J(J+1) \\ O_6^2 = \frac{1}{4}\{(11J_z^4 - 3J(J+1)J_z - 59J_z + (J_+^2 - J_-^2)\}_s \\ O_6^3 = \frac{1}{4}\{((11J_z^3 - J(J+1) - 38)(J_+^3 - J_-^3))\}_s \\ O_6^6 = \frac{1}{2}(J_+^6 + J_-^6) \end{cases}$$

For pure and dilute rare earths with c/a ratios close to the ideal value, we may thus expect a rapid $\frac{c}{a}$-dependence of A_{20}, and (2.4) may be a good approximation.

The calculation of the matrix elements of H_{CEF}, which are necessary to determine the CEF-splitting, is a standard calculation and the details are given in appendix 2. One important result is that only matrix elements $\langle m|O_{LM}|m'\rangle$ with $|m - m'| = M$ are non-zero.

The crystal field splitting is found (first order perturbation calculation) by diagonalizing the crystal field Hamiltonian, the eigenvalues giving the energy levels and the eigenfunctions giving the wavefunctions of the levels.

As H_{CEF} has a restricted number of non-zero matrix elements, the eigenfunctions are composed of at most three components. For example, for Er and Dy with $J = 15/2$, the following three types of mixings are found, all states being Kramers doublets:

1) $a|\pm15/2> + b|\pm3/2> + c|\mp9/2>$,

2) $a|\pm13/2> - b|\pm1/2> + c|\mp11/2>$,

3) $a|\pm7/2> + b|\mp5/2>$.

From the level scheme and the eigenfunctions follow the magnetic properties of the 4f ion, such as susceptibility and neutron scattering cross section.

Although the Hamiltonian (2.2) is based on an "external charge model" it is the most general CEF Hamiltonian for a 4f ion in hcp symmetry.

The specific property of this simple model is that the A_{LM}'s are determined completely by the surroundings of the 4f ions. If we neglect the small variance of $<r^L>$ through the series of heavy rare earths, this means that for a rare earth ion, diluted in a non-magnetic hcp-host, the parameters B_{LM}/α_L depend solely on the host.

Some comments on the external charge model are necessary.

First, the conduction electrons are not uniformly distributed but may be concentrated between the ions.

Second, the $5s^2p^6$ shell will have a screening effect, so that the 4f-shell will not feel the full value of the external charges.

By use of simple methods these complications may be contained within the framework of the external charge model. Furthermore because the screening effect of the $5s^2p^6$ shell must be nearly the same for all rare earths, this model still predicts that the parameters B_{LM}/α_L of a dilute rare earth depend almost solely on the diluent.

However, a third objection[8] makes it necessary to consider the possibility that these C_{EF}-parameters also depend on the 4f-ion itself. As neither the 4f-shell nor the 5d-shell are filled, the Pauli exclusion principle does not prevent the conduction electrons from having a 4f and 5d character, but the wave func-

tions of the conduction electrons must still be orthogonal to the
wave function of the 4f shell. The resulting correlation, the
strength of which will depend on the number of 4f electrons, makes
the 4f shell feel the CEF also "through" the conduction electrons.
So, if these correlation effects are strong enough, the observed
CEF interaction will depend both on the diluent and on the rare
earth.

2.3. Magneto-elastic Interaction

The magnetic interaction of 4f ions with lattice distortion
is closely connected to the CEF-interaction. The ME-interaction
arises from the shift in CEF-energy caused by a lattice distor-
tion.

For example, in Tb this shift is responsible for the magneto-
striction, the spontaneous lattice distortion produced by a macro-
scopic moment, which may be ferromagnetic or produced by an ex-
ternal field.

2.4. Indirect Exchange Interaction

The interaction between the 4f spins is caused by the con-
duction electrons through indirect exchange. Also dipole inter-
action exists, but it is negligibly small compared to the indirect
exchange. The mechanism[9] is that one 4f spin, by exchange inter-
action, polarizes the conduction electrons which in turn interact
with neighbouring 4f-spins. We shall denote the lattice sites of
4f ions $\underline{R}_L$ and their total angular momentum operators $\hat{\underline{J}}_L$. If the
spin-orbit coupling of the conduction electrons is neglected, the
total indirect exchange energy takes the simple Heisenberg form

$$H_{ff} = - \sum_{L>L'} \mathcal{J}(\underline{R}_L - \underline{R}_{L'}) \hat{\underline{J}}_L \cdot \hat{\underline{J}}_{L'} \qquad (2.5)$$

As a consequence of the shape of the Fermi surface, the ex-
change interaction is long-ranging and oscillating, and this
causes the rare earths to order magnetically in modulated, oscil-
latory structures.

From simple mean field theory (i.e. neglecting spin fluctu-
ations) one finds that J_L^α, the time-average cartesian components
of the 4f-spins in the ordered structure, will be proportional to

$\cos(\underline{Q} \cdot \underline{R}_L)$. Here $\underline{Q}$ is the point of absolute maximum of $\mathcal{J}(q)$, the Fourier transform of $\mathcal{J}(\underline{R}_L)$. This modulation appears in a certain range at and below a Néel temperature, which is given in mean field theory by

$$T_N = J(J + 1)(g - 1)^2 \frac{\mathcal{J}(Q)}{3k} \qquad (2.7)$$

analogous to ferromagnets.

In the heavy rare earths $\underline{Q} = \tau_{001} \, \zeta$, $\zeta = 0.1 - 0.3$, where $\tau_{001} = \frac{2\pi}{c}$ is the c-direction reciprocal lattice vector for the hcp structure. This means that on going from one hexagonal layer to the next, the modulation phase is increased with an interlayer angle $= Q \cdot \frac{c}{2}$, ranging from 20° (Tb) to 50° (Tm) just below T_N[10].

Also anisotropic exchange will give modulated structures. Together with the CEF-interaction the effect of the anisotropic exchange is to favour some of the spin directions, and thus to determine the actual form of the modulated structure.

However, when the mean spin components are sine-modulated with no net macroscopic magnetization, the structure may be described by a general expression, using a complex polarization vector $\underline{\mu}$:

$$\langle \underline{J}_L \rangle = \text{Re} \{ \underline{\mu} \, e^{i\underline{Q} \cdot \underline{R}_L} \} \, . \qquad (2.8)$$

The actual form is shown below for the two simplest cases, the spiral structure and the c-axis-modulated (CAM) structure:

	spiral	CAM
$\underline{\mu}$	$\begin{Bmatrix} \mu \\ -i\mu \\ 0 \end{Bmatrix}$	$\begin{Bmatrix} 0 \\ 0 \\ \mu \end{Bmatrix}$
$\langle \underline{J}_L \rangle$	$\begin{Bmatrix} \mu \cos \underline{Q} \cdot \underline{R}_L \\ \mu \sin \underline{Q} \cdot \underline{R}_L \\ 0 \end{Bmatrix}$	$\begin{Bmatrix} 0 \\ 0 \\ \mu \cos \underline{Q} \cdot \underline{R}_L \end{Bmatrix}$

$\mu = \mu(T)$ is temperature dependent, increasing from 0 as T is lowered from T_N.

This description also applies to the dilute rare earths. The exchange interaction just seems to be "diluted". The important parameter in this connection is the de Genne's factor

$$x = c(g-1)^2 J(J+1) \qquad (2.9)$$

where c is the atomic concentration.

As can be seen from fig. 2.2, both the Néel temperature T_N and the interlayer angle at T_N are nearly universal functions of x.

Saturation effects appear at temperatures sufficiently below T_N. For instance, a sine modulation may become square-like, and also the interlayer angle may change somewhat.

Like ferromagnetic structures, modulated structures also support magnons, i.e. spin waves consisting of deviations from the values of the ordered structure.
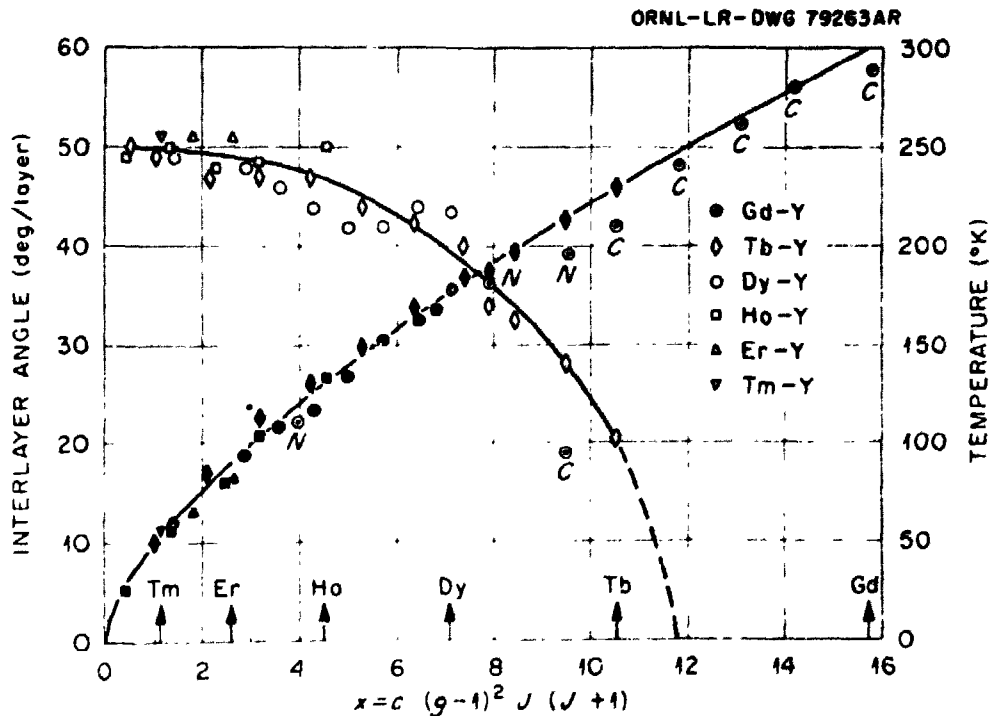

Fig. 2.2. The ordering temperature T_N and the interlayer angle at T_N are nearly universal functions of the average squared projection of S on J. From ref. 10.

- 15 -

2.5. Measurement of CEF in the Presence of Exchange

In general, the CEF levels break down more or less in the presence of indirect exchange interaction. However, above the Néel temperature and with moderate exchange, we may imagine the CEF levels to be fairly well defined, but as a consequence of the exchange the local CEF excitations, say from the ground state level, are replaced by collective excitations, excitons, with wavevector q and excitation energies $\hbar\omega = \hbar\omega(q)$ with dispersion. In addition, we may expect a broadening (finite lifetime) of these excitations due to the fluctuations of the exchange field (= the sum of all exchange interactions on a certain 4f ion).

In pure rare earth metals where the exchange interaction is strong, it is very difficult to measure the CEF parameters. At low temperature, where the CEF effects are clearest (only ground state level populated) the magnetic ordering dominates, and it is hard to distinguish between CEF and anisotropic exchange.

These complications are reduced in the dilute rare earths as all exchange interactions are much smaller than in the pure metals, simply because each 4f ion has far fewer 4f-ions as near neighbours, and T_N is accordingly low. However, even above T_N the CEF levels may be exchange-broadened by the fluctuating exchange field, perhaps enlarged by the random distribution of the rare earth ions. On the other hand, the oscillating long-range nature of the indirect exchange tends to make this effect small because the exchange field is some average over a large number of neighbours.

3. TECHNIQUE OF NEUTRON SCATTERING

As well known, one can observe the crystallographic structure and the lattice vibrations of a solid by neutrons scattered from the solid through nuclear interactions. Thermal neutrons (10-100 meV) are well suited because the de Broglie wavelength at these energies (1-3 Å) is of the same size as the interatomic distances. As neutrons carry a magnetic moment, they also interact magnetically with matter, so by neutron scattering one can also observe magnetic structures and magnetic excitations - neutron scattering is in fact the most direct way of observing these phenomena.

3.1. Neutron Spectrometer

The triple-axis crystal spectrometer for neutron scattering is sketched in fig. 3.1:
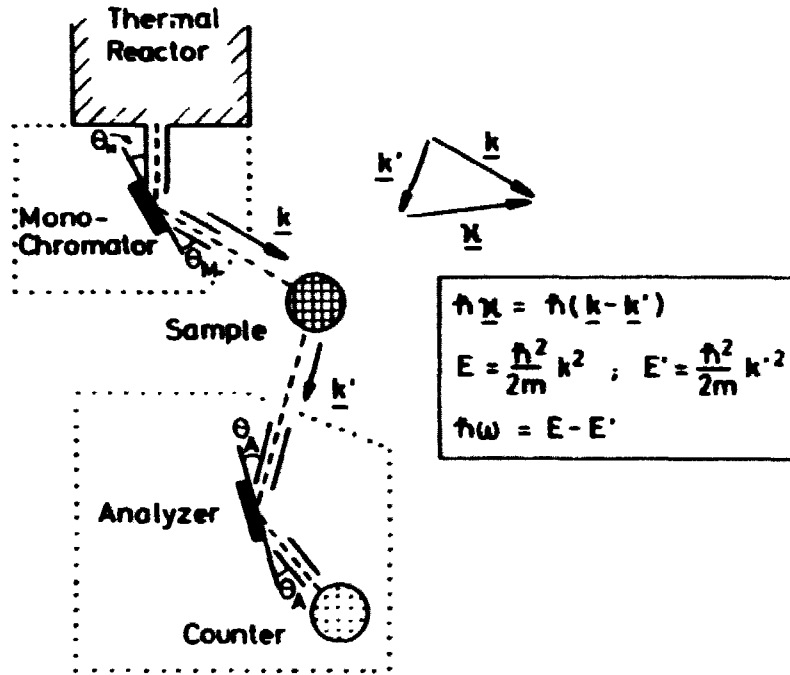

Fig. 3.1. Triple-axis crystal spectrometer. From the "white" reactor beam a monochromatic beam of neutrons is extracted by Bragg scattering from a monochromator crystal. The monochromatic, i - cident neutrons with wavevector $\underline{k}$ interact with the sample, and by the analyzer system (same principle as the monochromator system) and a counter the intensity is measured of neutrons scattered to wavevector $\underline{k}'$. $\hbar\underline{\varkappa}$ and $\hbar\omega$ are the momentum and energy transfer of the observed scattering.

The spectrometer has three variable scattering angles: at the monochromator (θ_M), at the sample, and at the analyzer (ϑ_A). In addition, the sample can be rotated around a vertical axis. The four axes of the Risø spectrometers are set by motors controlled by a computer that converts momentum and energy transfers $(\text{Å}^{-1}$ and meV) into the angle settings. Thus the experimentalist may work directly in $(\underline{\varkappa}, \hbar\omega)$ space after a calibration.

The intensity is measured for each setting by counting scattered neutrons for a preset time, or for a preset number of beam monitor counts (BMC). The beam monitor is a low efficiency counter, placed so that the incident monochromatic beam penetrates. Conse-

quently, use of preset BMC automatically corrects for fluctuations
in the reactor neutron flux. The number of neutron counts N has
a standard error $\sqrt{N}$, according to Poisson statistics (valid for
$N > 10$).

One disadvantage of the crystal monochromator system is the
order contamination, which has the effect that, if set for a wave-
vector $\underline{k}$, the monochromator system also lets through neutrons
with wavevectors $2\underline{k}$, $3\underline{k}$ ......, although with decreasing intensity.
The order contamination, which also occurs in the analyzer sys-
tem, may be removed by filters.

In this study use was made of graphite filters, which have
a very deep minimum in neutron transmission at 57.6 meV. In order
to use this minimum to reduce the second-order contamination, a
primary neutron energy of $57.6/4 = 14.4$ meV ($k = 2.636$ Å^{-1}) was
used. When scanning in the $(\underline{x}, \hbar\omega)$ space either the monochromator
or the analyzer system is kept fixed (except for very special
cases), and the filter is mounted in the fixed system.

As the reactor beam normally emerges from a water moderator
with a temperature around room temperature, the intensity of the
incident monochromatic neutron beam depends on the energy with
maximum intensity around 25 meV. However, after the installation
of the cold source (liquid H_2 around 30 K) at the DR 3 reactor,
the intensity of neutrons with energies as low as 5 meV has been
sufficiently raised to use them for scattering experiments that
require high intensity (such as scattering from CEF transitions).

3.2. Resolution

If we denote the flux of incident neutrons (per m^2 and second)
F_{inc} and denote the intensity of scattered neutrons (per second)
I_{sc} then the neutron spectrometer in principle measures the partial
scattering cross section

$$\frac{d^2\sigma}{d\Omega dE'} = \frac{1}{F_{inc}} \cdot \frac{d^2 I_{sc}}{d\Omega dE'}$$

where $d\Omega$ is an element of solid angle around the direction of $\underline{k}'$.

As explained in appendix 3, the instrument has a finite re-
solution and a total efficiency depending on the setting $(\underline{x}_0, \omega_0)$.
Thus the number of neutrons detected per second is given as a con-

volution integral of the cross section and a resolution function
$R(\underline{\varkappa}-\underline{\varkappa}_O, \omega-\omega_O)$, see eq. (A 3.4), which implicitly also depends
on $\underline{\varkappa}_O$ and ω_O. This function has approximately Gaussian dependence
on $(\underline{\varkappa}-\underline{\varkappa}_O)$ and $(\omega-\omega_O)$, while the implicit dependence on $\underline{\varkappa}_O$ and ω_O
is rather weak.

Appendix 3 gives the different "sources" of the resolution
from which it is possible to approximately calculate the resol-
ution function, e.g. the important pure energy resolution. The
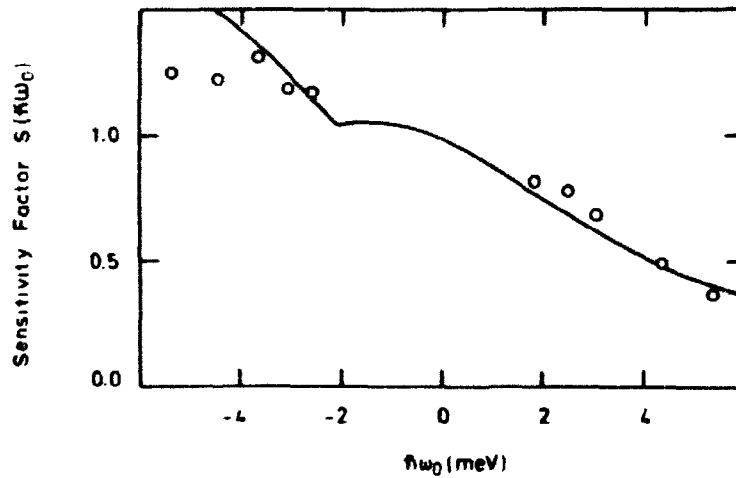most relevant results of the appendix are given here.

Fig. 3.2. Sensitivity factor normalized to unity at $\hbar\omega_O = 0$ for
fixed monochromator energy = 14.4 meV and pyrolytic graphite in
(002) reflection as analyzer. Varying resolution, counter ef-
ficiency, analyzer reflectivity and the factor $\frac{k'}{k}$ are included.
The sensitivity was checked by the integrated intensity (open
circles) of some phonons in the Y-2% Er sample at T = 300 K.

At the setting $\omega_O = 0$ the shape of the resolution function
may be determined experimentally. The resolution width in any
direction in the $(\underline{\varkappa}, \omega)$ space may be determined from a Bragg re-
flection, while the pure energy width, uncorrelated to $\underline{\varkappa}$, may be
measured by scattering from vanadium, a nearly purely incoherent
scatterer. In fig. 3.3 the resolution energy as a function of the
setting ω_O is shown for relevant cases, and the values for $\omega_O = 0$
are checked by V-scans. In most cases in this study the energy
resolution was around 1 meV using $E_{Mon} = 14.4$ meV. A much finer
resolution of 0.2 meV may be obtained at $E_{Mon} = 5$ meV, but at the
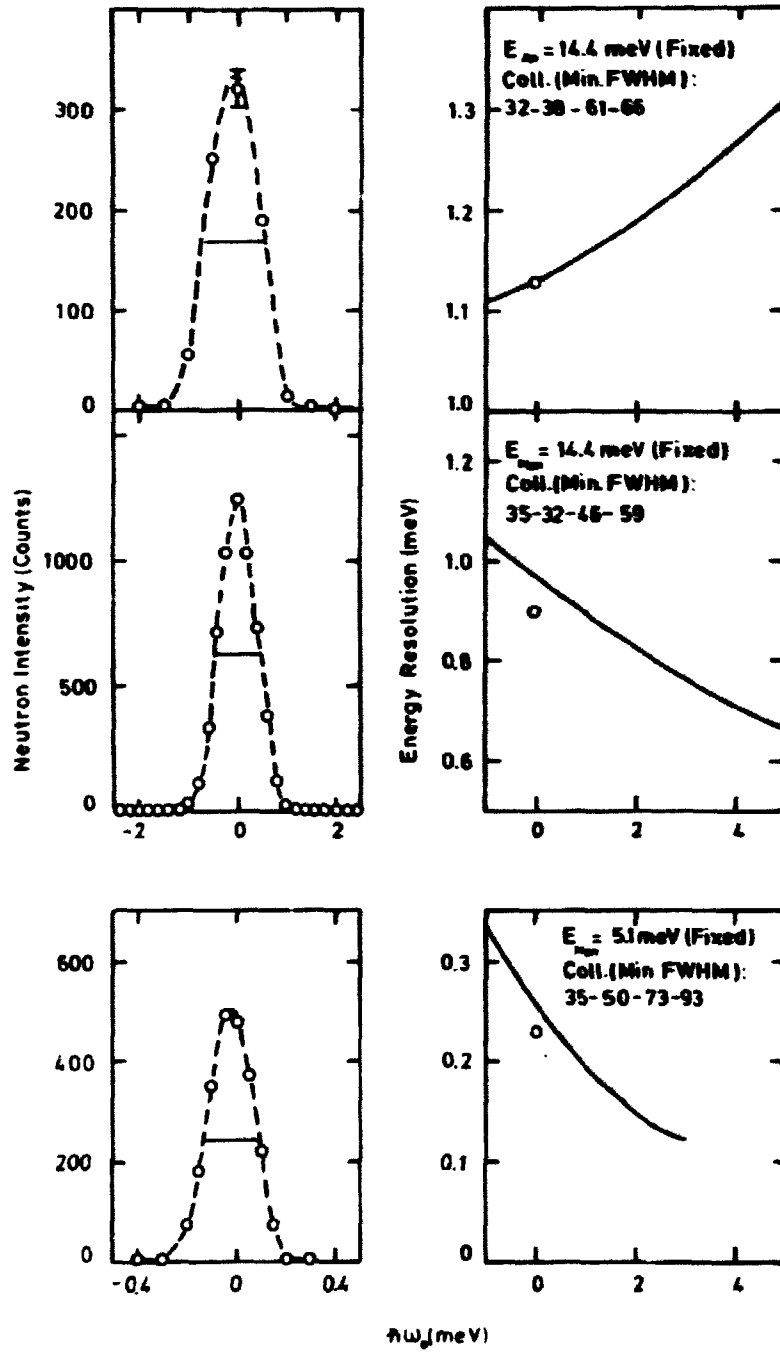cost of a drastic fall in the incident neutron intensity.

Fig. 3.3. Energy resolution widths for typical collimations and scan types. The (002) reflection of pyrolytic graphite is assumed for monochromator and analyzer. The widths are defined as the full width at half maximum (FWHM), as shown in the V-scans in the left column. The right column shows the widths as functions of $\hbar\omega$, and the widths of the corresponding V-scans are indicated. The use of 5 meV incident neutrons gives a very fine resolution of 0.2 meV.

In many cases only the total inelastic cross section is important, and not the shape, e.g. when the cross section is a sharp, δ-like function peaking around $\omega = \omega'$. In this case one may use the integrated intensity $u = \int I(\underline{n}_o, \omega_o) d\omega_o$, which is connected to the total inelastic cross section by a simple $\underline{n}$-independent sensitivity $s(\omega')$, see eq. (A 3.8). Figure 3.2 shows the sensitivity function valid for most of the measurements in this study.

3.3. General Scattering Cross Section

We will now go through the relevant neutron scattering cross sections linking the spectra of scattered intensity and the structures or excitations in the investigated sample. As unpolarized neutrons (random spin orientation) were used in this study, this sort of neutron beam will be assumed in the following.

The master formula for all scattering cross sections is the Born approximation. We denote all possible initial and final target states by $|\lambda\rangle$, P_λ (probability of state λ) and $|\lambda'\rangle$ and their energies by E_λ and $E_{\lambda'}$.

In the same manner the initial and final neutron states are $|k\sigma\rangle$ and $|k'\sigma'\rangle$ (σ = spin state, P_σ = probability of spin state). If we further denote the neutron mass by m and let $\hat{V}$ be the neutron-target interaction potential, the Born approximation to the partial cross section reads[11]

$$\frac{d^2\sigma}{d\Omega dE'} = \frac{k'}{k}(\frac{m}{2\pi\hbar^2})^2 \sum_{\lambda\sigma} P_\lambda P_\sigma \sum_{\lambda'\sigma'} |\langle \underline{k}'\sigma'\lambda'|\hat{V}|\underline{k}\sigma\lambda\rangle|^2 \delta(\hbar\omega + E_\lambda - E_{\lambda'}) . \quad (3.1)$$

This master formula is, of course, rather useless in practice unless specific cases are considered, and in the following the cross sections relevant to this study will be given.

3.4. Nuclear Bragg Scattering

Perhaps the best known kind of scattering is the elastic nuclear Bragg scattering from single crystals (the cross section is derived in standard test books). Let the crystal have reciprocal lattice vectors $\underline{\tau}$ and let it consist of N unit cells of volume V_o. The Bragg cross section is then

$$\left.\frac{d^2\sigma}{d\Omega dE'}\right)_{Bragg} = \frac{N(2\pi)^3}{V_o} \sum_{\underline{\tau}} \delta(\underline{\varkappa} - \underline{\tau}) | F_N(\tau) |^2 \delta(\hbar\omega). \qquad (3.2)$$

Two important features are observed: first, the scattering is purely elastic; second, scattering will only be observed when the spectrometer setting corresponds to a wave vector transfer $\underline{\varkappa}$ coincident with a reciprocal lattice vector $\underline{\tau}$ of the crystal.

In general, the intensity of a reflection depends on $\underline{\tau}$ through the structure factor

$$F_N(\underline{\tau}) = \sum_{\underline{d}} e^{i\underline{\tau}\cdot\underline{d}} \, b_{\underline{d}} \, \exp[-W_{\underline{d}}(\tau)] \, , \qquad (3.3a)$$

where $\underline{d}$ is the position of atoms inside the unit cell and $b_{\underline{d}}$ is the coherent scattering length of the atom at site $\underline{d}$. $\exp[-\overline{W}_{\underline{d}}(\tau)]$ is the so-called Debye-Waller factor, accounting for the "smearing out" of lattice points because of lattice vibrations. In the harmonic approximation we have

$$W_{\underline{d}}(\varkappa) = \frac{1}{2} \langle(\underline{\varkappa}\cdot\underline{u}_{\underline{d}})^2\rangle_{av.} \, , \qquad (3.3b)$$

$\underline{u}_{\underline{d}}$ being the atomic displacement from the mean position. With only one type of atom (3.3a) is simplified to $F_N(\tau) = b\, e^{-W(\underline{\tau})}\, G(\underline{\tau})$ with the geometric structure factor

$$G(\underline{\tau}) = \sum_{\underline{d}} e^{i\underline{\tau}\cdot\underline{d}} \, . \qquad (3.4)$$

A Bragg reflection is denoted by its Bragg indices (hkl). This means that $\underline{\tau}_{(hkl)} = h\,\underline{a} + k\,\underline{b} + l\,\underline{c}$, where $(\underline{a}, \underline{b}, \underline{c})$ are the basis for the reciprocal lattice. Table 3.1 gives the properties of the reciprocal lattice of an hcp structure and the geometrical structure factor $G(\underline{\tau}_{hkl})$.

The Bragg scattering is a result of the interference between scattered neutron waves and thus it involves the coherent scattering length b, corresponding to the mean neutron/nucleus interaction. Besides, the fluctuations (nuclear spin, isotopes) in this interaction cause the incoherent scattering. Due to the lack of interference, this scattering is uniformly distributed in all directions. Vanadium is a well known example of a nearly pure incoherent scatterer.

Table 3.1

Properties of the reciprocal lattice corresponding to the hcp structure. ΓA, ΓM, and ΓK are the group theoretical notation for the symmetry directions.

hkl	Direction of $\underline{\tau}$		Equivalent directions	$\lvert G(\tau)\rvert^2$
(0 0 1)	ΓA,	$\parallel$ c-axis		0
(0 0 2)	ΓA,	$\parallel$ c-axis		4
(1,0,0)	ΓM,	$\perp$ c-axis	$\pm$ (0,1,0)	1
			$\pm$ (1,-1,0)	
(1,1,0)	ΓK,	$\perp$ c-axis	$\pm$ (1,-2,0)	4
			$\pm$ (2,-1,0)	
(1 0 1)				3

3.5. Magnetic Scattering Cross sections

The magnetic scattering cross sections are somewhat more complicated because the magnetic moment, which interacts with the neutron, is distributed over an area comparable with the neutron wavelength, and also because of the directional properties of the magnetic interactions. In the dipole approximation, valid when $\varkappa \cdot r_s \ll 1$ (r_s = extent of an atomic spin), the magnetic scattering from an isolated atomic spin with conserved J (e.g. a 4f-ion) corresponds to a "magnetic scattering length" operator

$$p_0 \; g \; f(\varkappa) \underline{\hat{J}}^{\perp}$$

Here $\underline{J}^{\perp} = \frac{1}{\varkappa^2} \times \underline{\varkappa} \times (\underline{J} \times \underline{\varkappa})$ is the component of $\underline{\hat{J}}$ that is $\perp \underline{\varkappa}$, $f(\varkappa)$ is the magnetic form factor (= Fourier-transformed spin density) going to 1 when $\varkappa \cdot r_s \to 0$, g is the Lande factor and $p_0 = \frac{1}{2} \, 1.91 \, \frac{e^2}{m_e c^2} = 2.69$ fm is the scattering length per Bohr magneton. The magnetic scattering from a single crystal without lattice vibrations and with one type of magnetic atom, located at sites $\underline{R}_L$, is thus described by the cross section[13]

$$\frac{d^2\sigma}{d\Omega dE'} = (p_0 \; g f(\varkappa))^2 \frac{k'}{k} \sum_{\lambda'} P_\lambda \sum_{L,L'} e^{i\varkappa \cdot (\underline{R}_L - \underline{R}_{L'})} \times$$

$$\times \langle \lambda \mid J_L^{\perp} \mid \lambda' \rangle \cdot \langle \lambda' \mid J_{L'}^{\perp} \mid \lambda \rangle \, \delta(E_\lambda - E_{\lambda'} + \hbar\omega) .$$

- 23 -

This general expression is reduced when we consider the
specific cases, e.g. elastic scattering from an ordered structure
or inelastic scattering from crystal field transitions, that are
relevant here.

3.6. Scattering from a Modulated Magnetic Structure

A modulated magnetic structure described by e.g. (2.8) with
$\underline{Q} \neq \frac{1}{2} \times$ (any reciprocal lattice vector $\underline{\tau}$) has an elastic magnetic
cross section[10]

$$\left.\frac{d^2}{d\Omega dE'}\right)_{El.magn.} = \frac{N(2\pi)^3}{v_o} \frac{1}{4} \underline{\mu}^{\perp} \cdot \underline{\mu}^{*\perp} (p_o g\ f(\varkappa))^2 \ \cdot$$

$$\cdot \sum_{\underline{\tau}} G(\tau)\{\delta(\underline{\varkappa}-\underline{\tau}+\underline{Q}) + \delta(\underline{\varkappa}-\underline{\tau}-\underline{Q})\}\ \delta(\hbar\omega) \qquad (3.6a)$$

Similar to $\underline{J}^{\perp}$, $\underline{\mu}^{\perp}$ is the component $\perp \underline{\varkappa}$, and $G(\tau)$ is the geo-
metrical structure factor.

It is seen that the magnetic scattering is concentrated in
satellites $\underline{\varkappa} = \underline{\tau} \pm \underline{Q}$ around each nuclear Bragg reflection. Through
$\underline{\mu}^{\perp} \cdot \underline{\mu}^{\perp}$, the τ-dependence of the satellite intensities contains
information about the polarization in the structure. In the heavy
rare earths we have for the most frequent cases:

	$\underline{\mu}$	$\underline{\mu}^{\perp}\cdot\underline{\mu}^{*\perp}$
spiral	$(\mu,\ i\mu,\ 0)$	$\mu^2(1+\cos^2\theta)$
CAM	$(0,0,\mu)$	$\mu^2\sin^2\theta$

$$\theta = \sphericalangle(\underline{\varkappa},\ c\text{-axis}) \qquad (3.6b)$$

3.7. Inelastic Magnetic Scattering from Dilute Rare Earths

We now turn to a dilute rare earth alloy containing N_{RE} rare
earth ions. We shall assume that the rare earth concentration is
small enough to make the exchange interaction between the rare
earth ions negligible. In this case the spins $\underline{J}_L$ are uncorrelated,
and the cross section (3.5) reduces to N_{RE} (single-ion cross sec-
tion). We denote the energies and states of the crystal field
levels E_n and $|\Gamma_n \nu\rangle$, ν labelling the degenerate states of the

n'th level. The inelastic cross section, including the effect of lattice vibration, is then[14]

$$\left.\frac{d^2\sigma}{d\Omega dE'}\right)_{CEF} = N_{RE} \frac{k'}{k} A(\varkappa) \sum_{nn'} T_{nn'} \delta(E_n - E_{n'} + \hbar\omega) \qquad (3.7)$$

with

$$A(\varkappa) = \lfloor p_o \; g \; f(\varkappa) \rfloor^2 \; e^{-2W(\varkappa)},$$

and the transition probability

$$T_{nn'} = P_n \sum_{vv'} < v \; \Gamma_n \lvert \underline{J}^{\perp} \rvert \Gamma_{n'} \; v' > \cdot <c.c.> \; .$$

By definition, the ground state energy $E_o = 0$.

In an energy scan with $\underline{\varkappa}$ kept fixed, each transition $\Gamma_n \to \Gamma_{n'}$ will possibly give rise to a peak in the intensity spectrum at $\hbar\omega = E_{n'} - E_n$. Under the present assumption of negligible exchange interaction, the transition energies do not depend on the chosen wavevector transfer $\underline{\varkappa}$, but as $\varkappa$ is increased the transition intensities will fall smoothly in proportion to $\frac{k'}{k} \; f(\varkappa)^2 \; e^{-2W(\varkappa)}$.

Of special interest is the dependence of the intensity on the orientation of $\underline{\varkappa}$ with respect to the crystal axes. This dependence derives from $\underline{J}^{\perp}$. Through this dependence, additional information may be obtained on the wave functions $\lvert \Gamma_n \; v \rangle$.

As mentioned in chapter 2, the effect of residual exchange interaction will be 1) level broadening, and 2) dispersion (i.e. $\underline{\varkappa}$-dependence) of the excitation energies E_n. To estimate the dispersion, the energy scans need only be performed for $\underline{\varkappa}$-values throughout one Brillouin zone.

The <u>intensity</u> of some transition $\Gamma_n \to \Gamma_{n'}$ depends on the temperature through the probability P_n. At low temperatures, i.e. $kT << E_1$, a Kramers doublet ground state will have $P_o \sim \frac{1}{2}$ and other states $P_n \sim 0$. Such temperatures are experimentally preferable as only transitions $\Gamma_o \to \Gamma_n$ are observed, giving simple spectra with only neutron energy loss. With increasing temperature, the corresponding scattering intensities will fall in proportion to P_o.

In contrast, the scattering intensity from a phonon[12] with frequency ω_{p_1} **increases** both with T and $\varkappa$, as it is proportional to $\varkappa^2$ $(n(\omega)\pm\frac{1}{2})$, where $n(\omega) = [\exp(\frac{\hbar\omega}{kT}) - 1]^{-1}$ is the Bose population number. This dependence also applies to other types of lattice vibration such as local modes. Thus, scattering from CEF transitions can easily be distinguished from phonon scattering by the $\varkappa$ - and T-dependence of the intensity because it is totally different in the two types of scattering.

4. INELASTIC NEUTRON SCATTERING EXPERIMENTS WITH DILUTE RARE EARTH ALLOYS

This chapter reports on neutron spectroscopic investigations of the CEF levels in some dilute rare earth alloys.

4.1. Samples, Orientation and Temperature Control

Five samples were investigated; each consisted of one or two large single crystals with a total weight of 4-20 g. The detailed compositions and weights are given in table 4.1.

Table 4.1

Sample properties

The absorption is calculated for 14.4 meV neutrons taking the shortest route through the sample

Alloy[x]	Number of single crystals	Vertical cryst. axis	Total weight (g)	Absorption
Y-3.0% Dy	1	[110]	4.5	0.58
Y-1.1% Dy	1	[110]	9.2	0.34
Y-2.0% Er	2	[100]	22.5	0.18
Sc-2.0% Er	2	[100]	7.9	0.65
Lu-2.0% Er	2	[100]	10.7	0.79

[x)] Throughout this report all the percentages are atomic percentages.

The crystals were prepared by P. Touborg by arc-melting and strain annealing[15] of the alloy. Finally, suitable single crystals were spark-cut. A primary orientation within a few degrees was performed on an X-ray diffractometer.

The crystals were mounted on standard sample holders made of Al. The orientations of the samples are given in table 4.1, the vertical axis being perpendicular to the scattering plane and hence to κ.
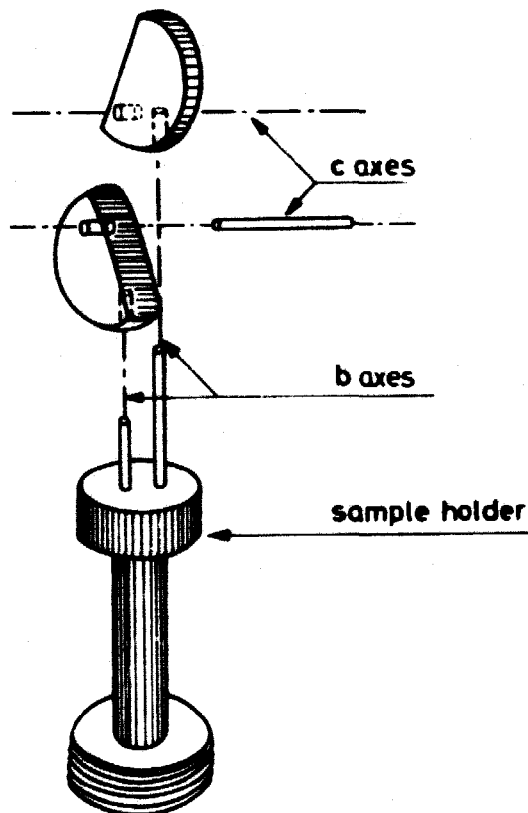

Fig. 4.1. Y-2% Er sample mounted on a standard sample holder of Al The two crystals were kept in orientation by means of Al pins inserted in spark-cut holes in the crystals.

Figure 4.1 shows the mounting of the Y-2% Er sample. As was the case for all the samples with Er, the two crystals were held correctly orientated with respect to one another by means of small Al-pins. In order to avoid neutron scattering from screws, etc., close to the crystals, such parts were shielded by the neutron-absorbing metal Cd.

During a neutron scattering experiment the sample on the sample holder was mounted in a He-flow-cryostat designed for neutron scattering. The sample was surrounded by He exchange gas, ensuring thermal equilibrium with the so-called temperature block that contained a heater and a thermosensor. An electronic temperature controller allowed the sample temperature to be kept

constant with an accuracy around 0.1 K, and temperatures down to 4.5 K could be reached. Calibrated Ge- and GaAs-thermosensors were used.

The cryostat was fastened to a large goniometer on the spectrometer sample table, allowing a final adjustment of the sample orientation. This was done by maximizing the intensities of two Bragg reflections with $\underline{\tau}$ in the scattering plane and perpendicular to one another: (002), (110) for the Er-samples and (002), (200) for the Dy-samples.

4.2. Diffraction Study of Magnetic Order

At the lowest possible temperature the samples were investigated for magnetic order. With $\hbar\omega = 0$ scans of the wavevector transfer $\underline{\varkappa}$ were performed through the points (in reciprocal space) of possible magnetic satellites $(h,k,l) = (0,0,2-\zeta)$, $(0,0,2+\zeta)$, $(1,1,\zeta)$ or $(1,0,\zeta)$ with $\zeta \approx 0.3$. The Y-3% Dy was clearly ordered at 5 K, and the Néel temperature was found to be $T_N = 9$ K,[3] fig. 1). A more detailed investigation of the magnetic order of this sample is reported in chapter 7.

The elastic scans for the remainder of the samples are shown in figs. 4.2, 4.3, 4.4 and 4.5. The resolution in $\underline{\varkappa}$-space can be seen from the width of the nuclear Bragg peak. Of these samples, only Lu-2% Er showed any magnetic order.

The satellites of Lu-2% Er persist nearly unchanged up to at least 20 K and presumably derive from small spots of rather concentrated Er (pure Er has $T_N = 85$ K[10]). From cross sections (3.2) and (3.6), it was possible to estimate the amount of "concentrated" Er by the intensity ratio r between the $(0,0,2-\zeta)$ satellite and the $(0,0,2)$ nuclear reflection. The coherent nuclear scattering length of Lu is $b_{coh} = 7.3$ fm. The ordered moment was assumed to be $g\mu = 4.3 \ \mu_B$, the maximum value in pure Er. Further, the orientation factor $(1 + \cos^2\theta)$ in eq. (3.6) is ≈ 2. The magnetic form factor was $f(\varkappa) \approx 0.9$. (The Tb value was used[19]). With these numbers and X being the concentration of magnetically ordered Er, we have

$$ r \triangleq \frac{I_{(0,0,2-\zeta)}}{I_{(0,0,2)}} = 2 \cdot \left(\frac{g\mu \cdot p_o \ f(\varkappa)}{2 \cdot b_{coh}}\right)^2 \cdot X = 1.05 \ X \ . $$
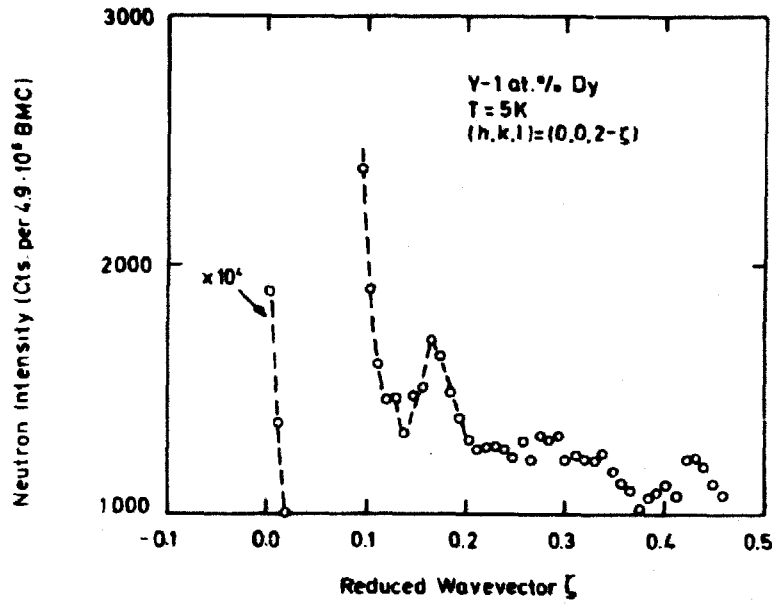
Fig. 4.2. Elastic scattering from Y-1.1% Dy for magnetic order.
No (0, 0, 2-ζ) satellite is seen around ζ = 0.3. The peak at
ζ = 0.17 is caused by spurious (100) reflections from small,
misoriented grains.

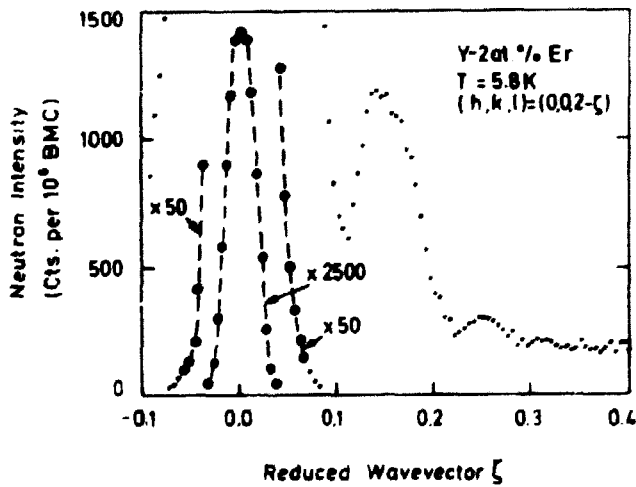Fig. 4.3. Elastic scattering from Y-2% Er for magnetic order. No
(0, 0, 2-ζ) satellite is seen around ζ = 0.3. The peak at ζ =
0.15 is caused by spurious (100) reflections from small, mis-
oriented grains.

Experimentally, $r = 6 \cdot 10^{-4}$, so $X = 5.7 \cdot 10^{-4}$. This is an upper limit because the neutrons have a finite penetration depth at the strong $(0,0,2)$ Bragg reflection. Thus less than 3% of the Er takes part in the magnetic ordering and this is negligible for inelastic neutron scattering.
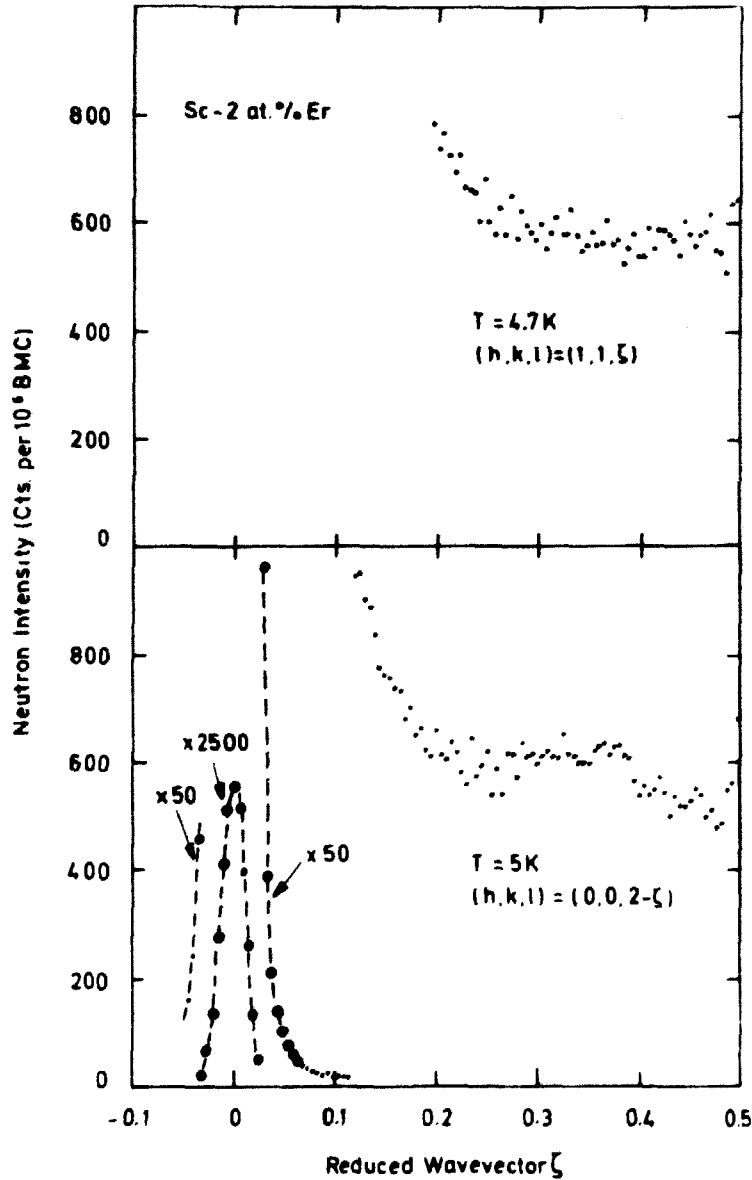
Fig. 4.4. Elastic scattering from Sc-2% Er for magnetic order. Neither $(1, 1, \zeta)$ nor $(o, o, 2-\zeta)$ satellites are seen for $\zeta \gtrsim 0.3$.
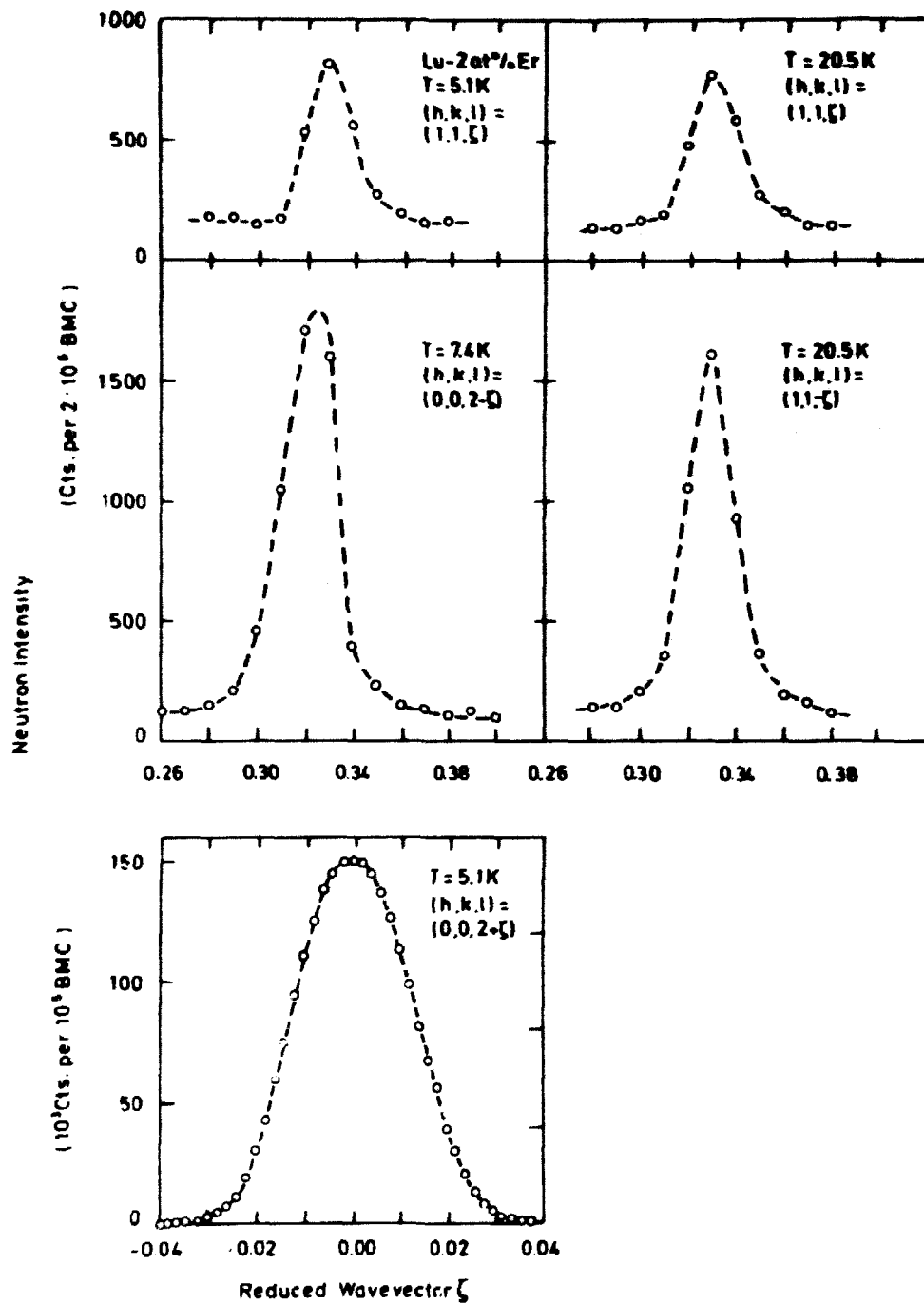
Fig. 4.5. Elastic scattering from Lu-2% Er for magnetic order.
Clear (0, 0, 2-ζ), (1, 1, ζ) and (1, 1, -ζ) satellites are seen
for ζ = 0.31, at least up to T = 20 K. As shown in the text, the
satellites are presumably caused by ordering in small, concentrated
Er regions formed by less than 3% of the Er atoms.

4.3. Inelastic Scattering Spectra

For each sample the main inelastic experiment consisted of an energy ($\hbar\omega$) scan from -2 to 6 meV, approximately. Unless stated otherwise, the monochromator energy was fixed at 14.4 meV, filtered with graphite.

The wavevector transfer $\underline{\varkappa}$ was kept fixed at a value between 1.6 Å^{-1} and 2.0 Å^{-1}, and except for the Y-3% Dy sample two directions of $\underline{\varkappa}$ were used: 1) ΓA and 2) ΓM or ΓK. It was hoped that the difference in intensity between the two corresponding spectra would give additional information on the CEF-states. Unfortunately, for most of the samples the two spectra could not be compared directly because of the rather large neutron absorption (see table 4.1).

From the diffraction scans it was seen that no spurious scattering occured at $\hbar\omega$ = o, and relevant phonon dispersion measurements[16,17,18] ensured that no phonon scattering could occur in the part of the ($\varkappa$,ω) space where the inelastic scans were performed.
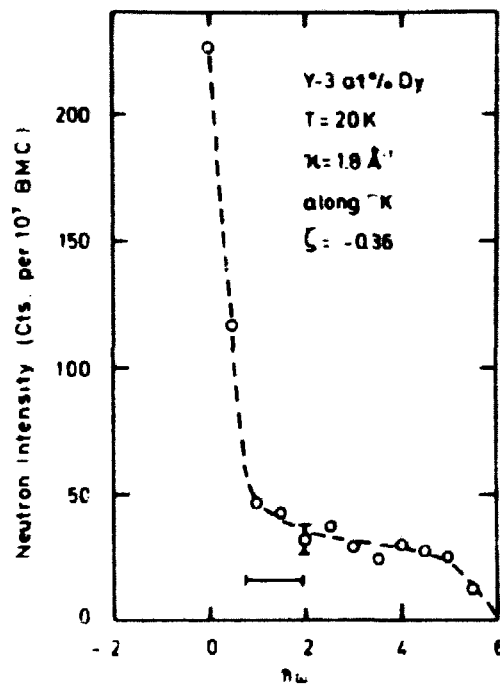

Fig. 4.6. Inelastic scattering spectrum from Y-3% Dy above T_N. The spectrum was taken with a fixed analyzer energy of 14.4 meV filtered with graphite. The energy resolution (FWHM) is denoted by a horizontal error bar, while the vertical error bar shows the statistical standard error of the single neutron counts. The dashed line is a guide-to-the-eye. These signatures are used in the remaining inelastic scattering spectra.

Figure 4.6 shows the spectrum from the Y-3% Dy above the or-
dering temperature. Apart from the incoherent nuclear scattering
at $\hbar\omega = 0$, no structure can be seen, only some very broadened in-
tensity, and no information on the CEF levels was gained. It is
thought that this is due to a large level boradening caused by
the strong exchange interaction that was also responsible for the
high ordering temperature.

Spectra from the Y-1.1% Dy sample are shown in[3] fig. 4. As
was the case for the main spectra from the remainder of the samples,
at the low temperature around 5 K only transitions from the ground
state level to higher levels were observable. On the side of the
elastic incoherent peak a "shoulder" is seen around 1.4 meV. This
is believed to be caused by the CEF transition $\Gamma_0 - \Gamma_1$. As expected,
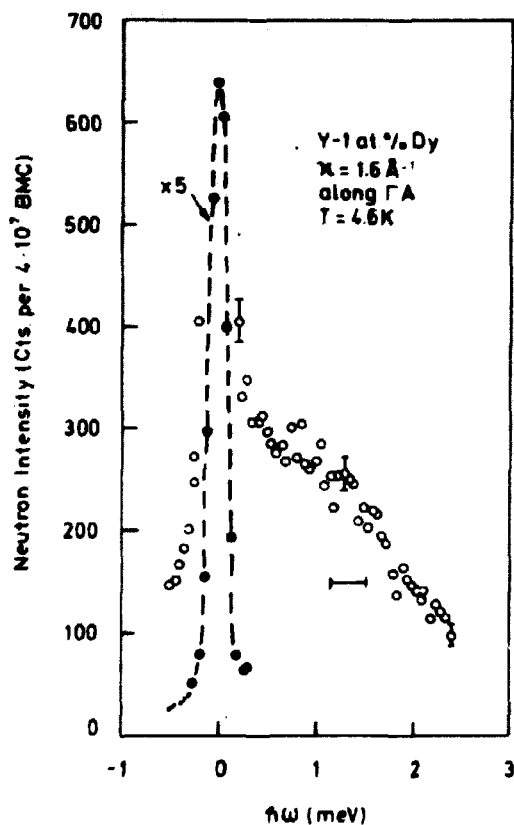
Fig. 4.7. Inelastic scattering spectrum from Y-1.1% Dy with
0.2 meV resolution. The observed width of the shoulder is thus
purely intrinsic. The fine resolution was obtained by using a
fixed monochromator energy of 5 meV, filtered with Be at 77 K.
The (high flux) reactor beam was obtained from the cold source at
the DR 3 reactor.

at T = 30 K the intensity of the shoulder was decreased; thus
although it was impossible to resolve the shoulder completely by
a finer resolution (see fig. 4.7), there is no doubt that the
scattering is caused by a CEF transition. This is further proved
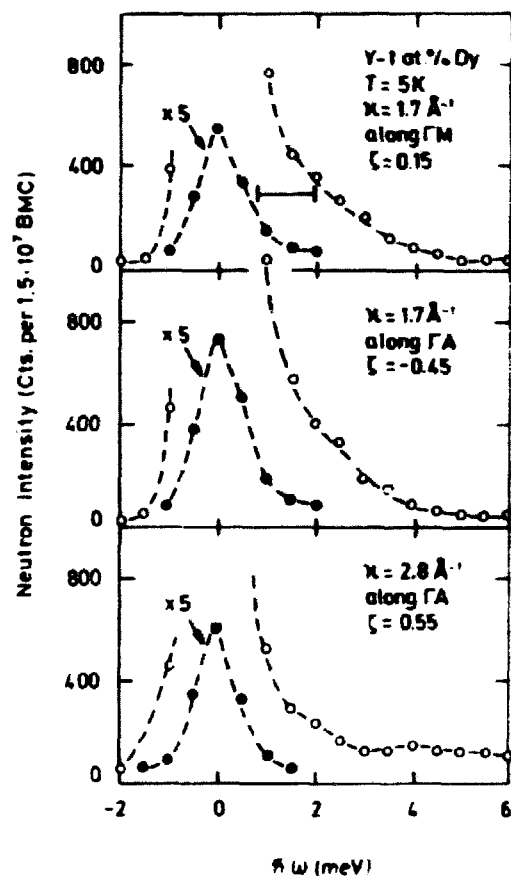by the decreasing intensity with increasing κ, as seen from the
spectra in fig. 4.8.

Fig. 4.8. κ-dependence of inelastic scattering spectrum from
Y-1.1% Dy. The spectra are measured with a fixed analyzer energy
of 14.4 meV in connection with a graphite filter. The reduced
wavevectors ξ and ζ are defined by (h, k, l) = (1, 0, 0) -
(ξ, 0, 0) and (h, k, l) = (0, 0, 2) + (0, 0, ζ).

Although not too clear, these spectra also indicate that the dis-
persion is at most 0.4 meV.

The inelastic scattering experiment with the Y-2% Er sample
was the most satisfactory of the five measurements. All the fea-
tures expected from CEF transitions were displayed very clearly.
The results were published in [2].

The 5 K spectra are shown in fig. 1 of this paper. We see three clearly resolved peaks caused by transitions from the CEF ground state level to three excited levels at approximately 2.1, 3.8, and 5.1 meV. As this alloy has a small neutron absorption, the intensities of the two spectra with $\underline{q}$ ΓA and $\underline{q}$ ΓK may be compared directly. The validity of this comparison was further demonstrated by a measurement of intensity versus sample orientation (2) fig. 2) in close agreement with the prediction of the cross section, eq. (3.7).

Thus the difference in elastic intensity between the two spectra seems to be caused by elastic magnetic scattering from the CEF ground state, formally a Γ_0-Γ_0 transition. The effect of raising the temperature to 20 K is shown in fig. 4.9.
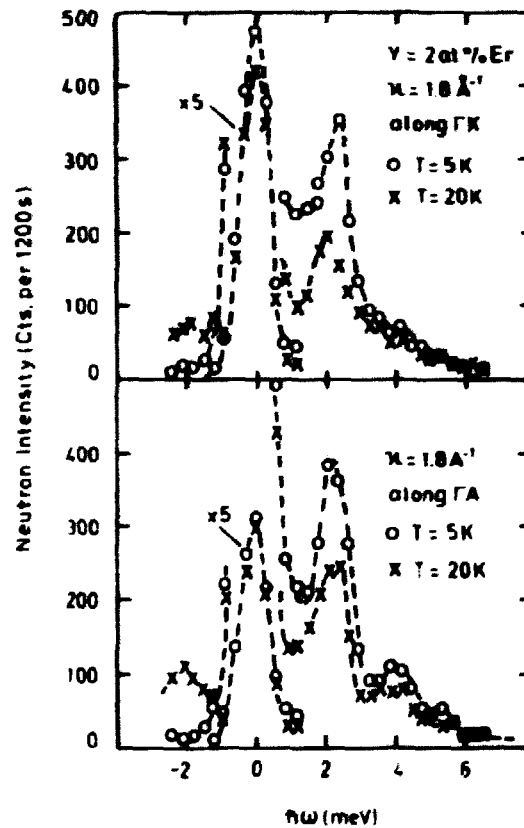

Fig. 4.9. Temperature dependence of inelastic scattering spectra from Y-2% Er. As the temperature is raised from 5 to 20 K, a peak at 2.1 meV neutron energy gain appears at the expense of the intensity in the neutron energy loss part of the spectra.

The intensities of the $\Gamma_0 \to \Gamma_n$ transitions are reduced, but at $\hbar\omega =$ -2.1 (neutron energy gain) there appears a peak caused by the $\Gamma_1 \to \Gamma_0$ transition. This transition becomes visible as Γ_1 becomes populated (P_1 is increased) at 20 K. The interpretation of the difference in elastic intensity at 5 K is supported by the fact that raising the temperature reduces this intensity only in the spectrum with $\kappa \| \Gamma K$. The peak at $\omega = 2.1$ meV was measured at 4.5 K for different κ-values (fig. 4.10) and no dispersion was observed.
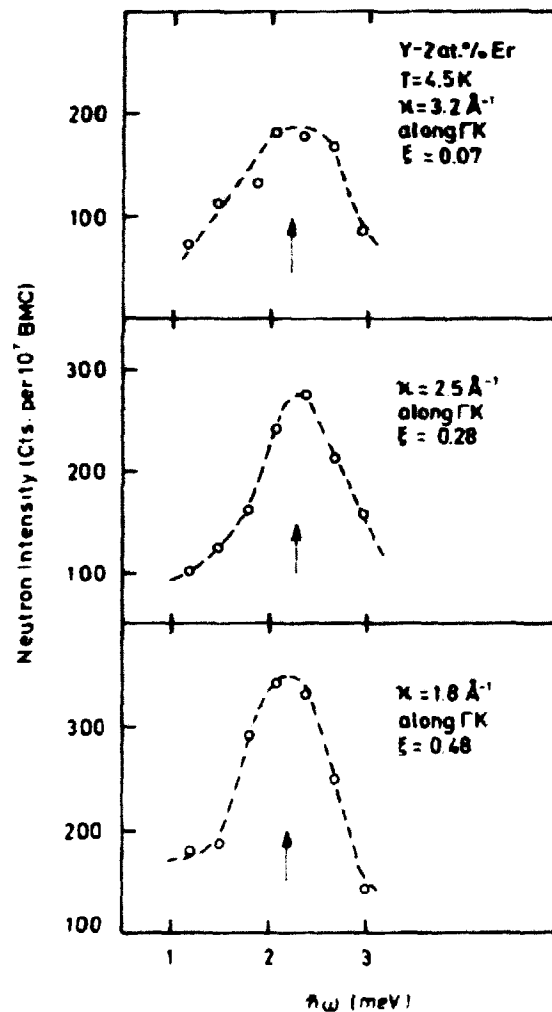
Fig. 4.10. κ-dependence of the peak at $\hbar\omega = 2.1$ meV ($\Gamma_0 \to \Gamma_1$ transition) in Y-2% Er spectra. As κ is increased no dispersion is observed but the intensity decreases. The reduced wavevector ζ is defined by (h, k, l) = (1, 1, 0) - (ζ, ζ, 0).

As expected, the intensity decreased approximately in proportion to $f(x)^2$. (The form factor for Tb was used[19]).

The Sc-2% Er and Lu-2% Er samples had a rather large neutron absorption, thus yielding less detailed results. The main spectra are shown in [3], figs. 2 and 3. In Sc-2% Er transitions to the first and second excited levels were observed ($\hbar\omega$ = 2.5 and 4.4 meV). The Lu-2% Er spectra showed only one clear transition peak ($\hbar\omega$ = 2.1 meV), but the analysis indicates a further small peak around $\hbar\omega$ = 4 meV.

The checks for the expected alterations with increasing x and T for the two samples are shown in figs. 4.11 and 4.12, and no dispersion was observed.
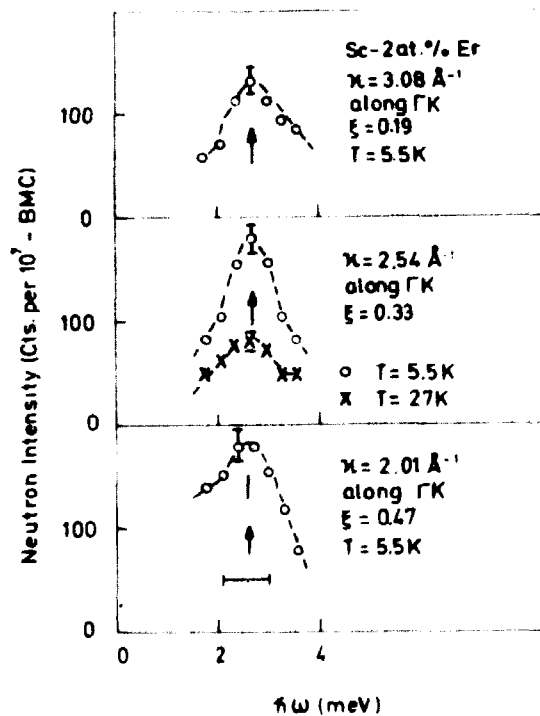

Fig. 4.11. x- and temperature dependence of the peak at 2.6 meV ($\Gamma_0 \to \Gamma_1$) in the Sc-2% Er spectra. No significant dispersion is seen, but the intensity shows a tendency to decrease with increasing x or T. ξ has the same meaning as in fig. 4.10.

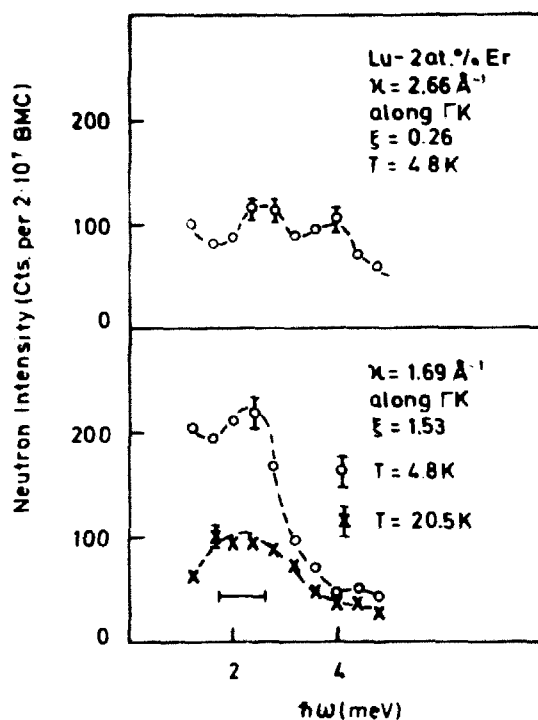Fig. 4.12. Temperature and x-dependence of the peak at 2.15 meV $(\Gamma_0 \rightarrow \Gamma_1)$ in the Lu-2% Er spectra. The behaviour is similar to that of the Er-alloys except for the peak at 4 meV in the $\xi = 0.26$ spectrum. No phonons exist at this point, but as a small part of the Er is ordered this peak may be caused by magnons. ξ has the same meaning as in fig. 4.10.

5. ANALYSIS OF INELASTIC SCATTERING EXPERIMENTS

In principle, one may determine all 4 CEF parameters of the Hamiltonian (2.2) from inelastic neutron scattering spectra. In this study the aim of the analysis was more modest because suggested values were available, deduced from magnetization measurements. As reported, Høg and Touborg measured the susceptibilities of Tb, Dy, Er and Ho diluted in Y[20,21], Lu[22] and Sc[23], and from the temperature dependence they deduced the CEF parameters B_{20}/α, B_{40}/β, B_{60}/γ and B_{66}/γ.

A striking result was the uniqueness of the parameters obtained from the alloys containing Dy.

5.1. Least Squares Fit

The main neutron scattering spectra, measured at low temperature (T ∿ 5 K) and low momentum transfer (x ∿ 1.8 Å^{-1}), were analyzed as described below. In a model expression, representing

the "experimental outlook" of the scattering cross section eq.
(3.7)

$$I(\omega) = \sum_n \frac{U_n \cdot S(E_n)}{1.0645 \cdot W_n} \exp\left(-\left(\frac{\hbar\omega - E_n}{0.6006 \cdot W_n}\right)^2\right) + B, \qquad (5.1)$$

each peak of the spectra was, above a background B, represented
by a Gaussian distribution with transition energy E_n, width
(FWHM) W_n and intensity U_n. As the instrumental sensitivity $S(E_n)$
was included, the intensities U_n with $n>0$ were proportional to
the transition probability factors T_{on} when absorption effects
were disregarded. Besides magnetic intensity, U_o (elastic peak)
also contained nuclear intensity. The expression (5.1) was fitted
to the measured spectra by a least squares fitting procedure (see
appendix 1). Depending on the quantity of detail in the spectra,
the fitting was performed for each alloy in one of two ways as
described below.

5.2. Y-2% Er

The spectra of this alloy were little influenced by absorp-
tion. Moreover, as four magnetic peaks were seen with $\underline{\kappa}$ in two
directions, a simultaneous LS-fit to both spectra was performed,
where the CEF parameters were determined directly. The details
of this procedure are described in [2]. In principle, the model
expression (5.1) was used, but E_n and U_n were given in terms of
the CEF parameters and a common scaling factor. The CEF parame-
ters deduced agreed with the magnetization results within the
uncertainty. In addition, the first 3 excited levels were found
to have an intrinsic width of 1.1 meV, presumably due to ex-
change broadening. As can be observed directly ([2] fig. 1) the
fit was statistically poor (χ^2 21), because the intensity at
the 2.1 meV peak could not be reproduced properly by the model
expression (5.1). Further, the best fit value of the magnetic
scaling factor S was 30% higher than expected from scattering
from a V sample. As the elastic intensity varied as $\cos^2\psi$ with
the crystal rotating angle (see [2] fig. 2) this discrepancy
cannot be due to the absorption but must be ascribed to a modi-
fication of the 4f wavefunctions ψ_n and hence U_{on}. This could

be caused by interaction of a given 4f shell either with the conduction electrons or maybe with the $5s^2p^6$ outer shells.

5.3. Y-1% Dy, Sc-2% Er and Lu-2% Er

The spectra from these samples were analyzed separately by LS-fitting directly using the model expression (5.1). Thus the LS-fits only served to extract the most accurate values and uncertainties of the energy, width and intensity of the observed transitions to be compared to the magnetization results. This course was taken because the spectra, which were affected by absorption or which had only one observed transition, were judged not to contain enough information for an independent determination of CEF-parameters. For the Sc-Er and Lu-Er alloys, a further reason was that the published magnetization CEF parameters gave transition energies that at a first glance seemed to agree well with the scattering spectra.

Table 5.1

Deduced parameters of observed CEF transitions $|_0 \rightarrow |_n$

	Direction of $\underline{\kappa}$	n	E_n (meV)	W_n (meV)	σ_n	U_n	χ^2
Sc-2% Er	A	1	2.58±.05	1.83±.22		310±28	
							1.05
		2	4.45±.09	1.17±.16		122±25	
	F	1	2.55±.06	1.59±.23		390±41	
							2.7
		2	4.33±.2	1.2±.4		89±36	
	Mean of	1	2.56±.06	1.7±.2	1.50±.22		
	A, F	2	4.45±.09	1.18±.16	0.95±.19		
Lu-2% Er	K	1	2.14±.04	1.8±.1	1.6±.1	351±18	
							1.7
		2	$4.0^{*)}$	1.1±.3	0.9±.4	38±12	
Y-1% Dy	A	1	1.31±.20	1.35±.45	1.1±.5	-	2.8

For Sc-2% Er, the "best"values of E_n and W_n are the mean of the "A"and the "F"-values. The intrinsic widths σ_n are defined by $W_n^2 = (W_{ins}(E_n))^2 + \sigma_n^2$.

*) E_2 was kept fixed during the fitting at the value deduced from magnetization. χ^2 was raised to 5 when using a model function where the $|_0 \rightarrow |_2$ transition was simply omitted. This fact gives evidence for the existence of this transition in the spectrum.

reduced wavevector ζ = .275, corresponding to an interlayer turn-
-angle of ω = 49.5°. The intensity ratio between the $(002)^-$ and
the $(100)^-$ satellites was found (corrected for resolution effects)
to be 10.2. According to eq. 3.6, this ratio is 0 for CAM-struc-
tures and 8 for a spiral. Ascribing the deviation from 8 to the
absorption of the sample, it is concluded that the structure is
a spiral.

The magnitude of the ordered moment (μ in eq. 3.6) is found
from the intensity ratio between the $(002)^-$ satellite and the
(002) nuclear Bragg reflection because the absorption is nearly
the same for $(002)^-$ and (002). With $b_{coh,Y}$ = 7.9 f.m., the same
procedure was used as described for the Lu-2% Er sample in chapter
4.

From the temperature dependence of the $(002)^-$ satellite
(fig. 6.2, following section), the "saturated" (T→0) intensity
ratio, corrected for resolution effects, is found to be

$$\left. \frac{I_{(002)^-}}{I_{(002)}} \right)_{sat.} = 7.7 \cdot 10^{-3} \ .$$

Using the magnetic form factor $f(\kappa) \approx 0.9$, the experimental
value for the ordered moment μ may be expressed as

$$\mu \cdot x = 2.3 \ \mu_B$$

where x is the fraction of Dy atoms taking part in the ordering.
As finite penetration depth at the (002) reflection (extinction)
has been neglected, the true value may be even lower.

It is natural to compare these results with the CEF ground
state found for Y-1.1% Dy that is dominated by the term $0.99|M_J =$
$\pm1/2\rangle$. In accordance with the observed spiral structure, this
ground state predicts the moment to lie in the basal plane, but
in contrast to the Dy^{3+} free spin of 10 μ_B the maximum basal plane
moment of the ground state is 5.2 μ_B, "quenched" by the CEF. How-
ever, as the indirect exchange has a magnitude (T_N = 9 K) compar-
able to the energy of the first excited CEF-state (15 K), admix-
ture of this state may increase the saturated magnetization to
about 7 μ_B. Thus the fraction x is around 15%.

6.2. Temperature Dependence of (002)⁻ Satellite

At temperatures from 2.2 to 9.5 K, the (002)⁻ satellite was investigated by transverse diffraction scans ($\hbar\omega = 0$) as seen in fig. 6.1. The measurements below 4.5 K were performed with the sample in a He pump cryostat, while a flow cryostat was used at the higher temperatures.
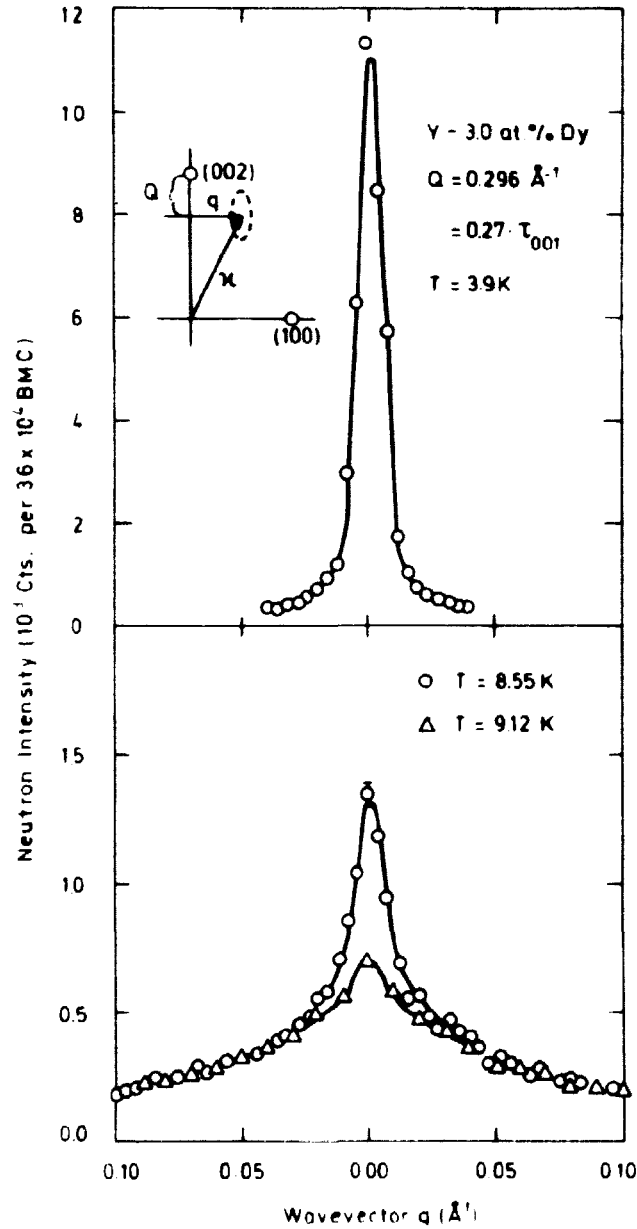
Fig. 6.1. Transverse neutron diffraction scans of the (002)⁻ magnetic satellite. As seen at the bottom, near T_N the scan is dominated by critical-scattering-like wings. In the insert at the top, the scan in reciprocal space is illustrated and the orientation of the resolution ellipse is indicated.

The peak intensity of the satellite decreased as the temperature was raised until the satellite disappeared at $T_N \approx 9.12$ K. This gradual fading away is a typical second-order phase transition.

At the low temperatures the width of the satellite was small, determined by the instrumental resolution, but approaching T_N the satellite became increasingly dominated by "wings", much broader than the resolution, as seen in fig. 6.1. This is rather similar to the so-called critical scattering, caused by short-range spin order, that is observed close to the ordering temperature in concentrated magnetic systems (e.g. in Tb[24]).

In order to distinguish between the wings and the sharp "Bragg part" of the satellite, the scans were analyzed by a least squares fit with the following model expression:

$$I(q) = B + P_B \, R(q) + \frac{P_L}{1+(\frac{q}{W_L})^2} \qquad (6.1)$$

where B is a constant background and R(q) is the experimental resolution function (see upper part of fig. 6.1), approximately described by

$$R(q) = .726 \, \exp(-\frac{q^2}{\sigma_1^2}) + .274 \, \exp(-\frac{q^2}{\sigma_2^2}) \qquad (6.2)$$

$$\sigma_1 = 5.35 \cdot 10^{-3} \, A^{-1}, \quad \sigma_2 = \sqrt{5} \, \sigma,$$

As normal for critical scattering, the "wings" were represented by a Lorentzian with a full width at half maximum W_L.

The results of the least squares fit are shown in fig. 6.2. The Bragg intensity seems to saturate at 2 K, and in the range 3 K < T < 8 K it decreases nearly linearly until it goes to zero at the Néel temperature 9.12 K with a decreasing slope.

The "critical scattering" has a nearly constant width of 0.035 A^{-1} and a broad intensity maximum around 6 K.
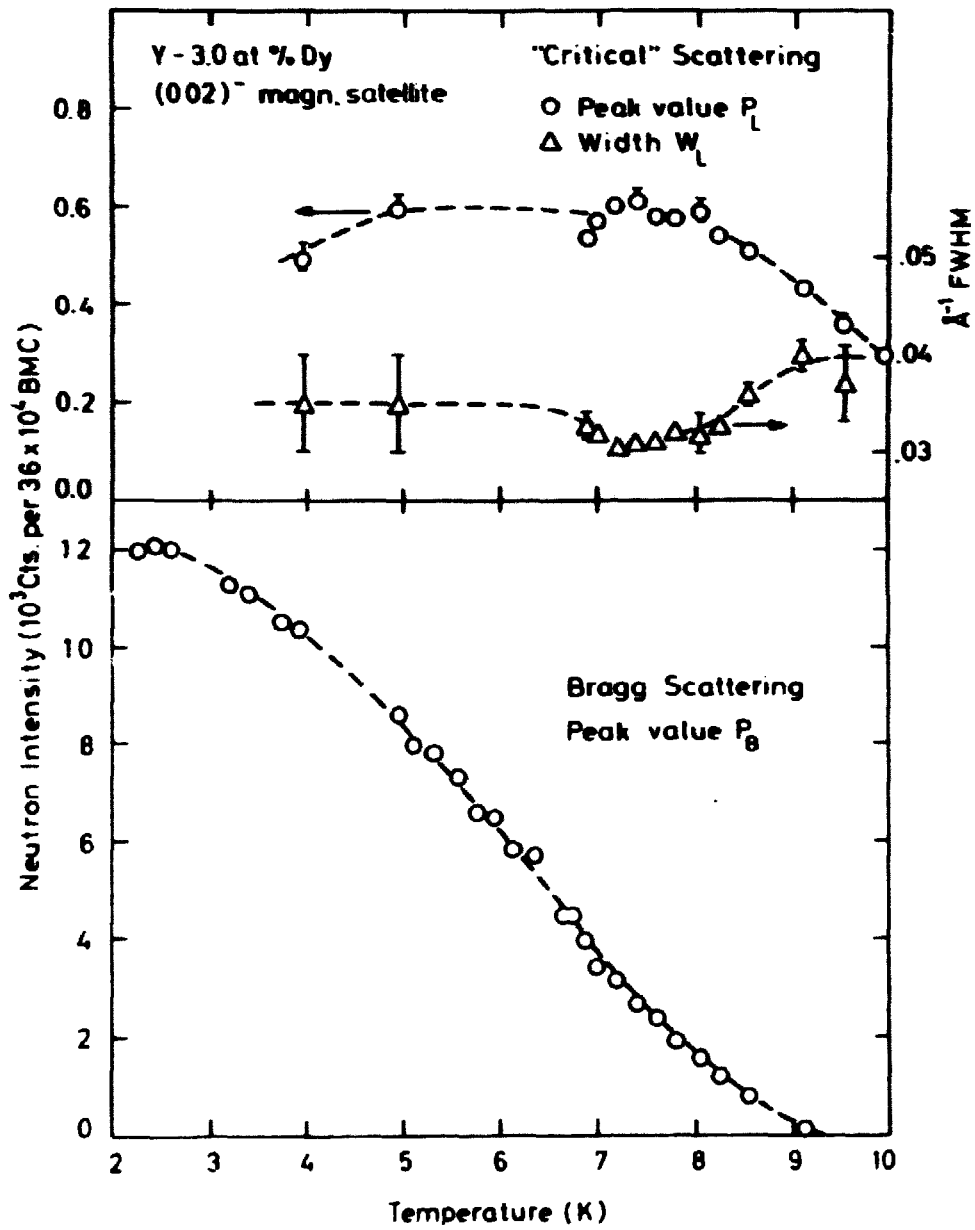
Fig. 6.2. Temperature dependence of the (002)⁻ magnetic satellite: Peak value and width of "critical scattering" and peak value of resolution-shaped Bragg scattering. The two components of the scattering have been separated by least squares fitting with a suitable model function (see text).

6.3. Example of Concentrated "Magnetic" System: β-Brass

For comparison, the corresponding behaviour of a concentrated system is discussed. β-brass is a nearly 50 at.% Cu - 50 at.% Zn alloy which goes from an ordered to a disordered bcc phase when the temperature is raised through T_c = 740 K. Although not magnetic, this phase transition is quite similar to that of a spin 1/2 pure antiferromagnetic system. (Using the notation of chapter 2: $Q = a$ of the cubic reciprocal lattice). This is the case because the configurational energy of β-brass, associated with the different types of nearest neighbours: Cu-Cu, Zn-Zn or Cu-Zn, has the form of an exchange energy. One lets S_1 = 1/2 or - 1/2 correspond to site 1 being occupied by a Cu or a Zn atom, respectively, and only nearest neighbour interaction is assumed. The simplicity of this so-called Ising system has made detailed theoretical predictions possible, and experimental results have been obtained by neutron diffraction [25,26].

In accordance with theory, the equivalent magnetization goes to zero as $\mu \propto (T_c-T)^\beta$, β = 0.293, that is the diffraction "satellite" intensity $I \propto \mu^2(T_c-T)^{2\beta}$ goes to zero with an infinite slope. At lower temperature, the measured magnetization is not in complete agreement with theory on an absolute scale, as first imagined on the basis of earlier neutron diffraction results, but up to 10% larger.

Again in agreement with theory, the critical scattering is observed to vary with a peak intensity $I_p \propto |T-T_c|^{-\gamma}$ and width $w \propto |T-T_c|^{-\nu}$, γ = 1.25, ν = 0.65.

6.4. Satellite Temperature Dependence Compared to Concentrated Systems

In the temperature dependence of the satellite of Y-3% Dy, although only observed by scans in the (100)-direction, two features have been observed that differ clearly from concentrated systems:

1) The Bragg intensity does not go to zero with infinite, but with decreasing slope, and

2) The "critical" scattering is rather temperature independent with no distinct maximum and no narrowing at the Néel temperature.

It is not quite clear what causes these effects, but it may be fruitful to see them in the light of recent spin-glass experiments by Sarkissian and Coles[27]. According to their results, Y_{1-x}-Dy_x alloys with x less than a "critical" concentration of 2.6% display a short-range ordered spin-glass phase rather than the magnetic spiral phase seen in more concentrated alloys. It is tempting to see the very "soft" spiral-to-disorder transition observed in Y-3% Dy as a consequence of the proximity to the critical Dy concentration.

Another, less exciting, explanation is that variations in the local Dy-concentration may "broaden" the Néel temperature. A 10% T_N-broadening is required to give the observed temperature dependence of the Bragg intensity. This effect is made likely by the fact that only 10-20% of the Dy atoms seem to take part in the ordering.

7. ACKNOWLEDGEMENTS

REFERENCES

1) P. Touborg and J. Høg, Phys. Rev. Lett. **33** (1974) 775-778.

2) O. Rathmann, J. Als-Nielsen, P. Bak, J. Høg and P. Touborg, Phys. Rev. **B10** (1974) 3983-3987. Enclosed. Errata: The direction ΓM should be replaced by ΓK.

3) O. Rathmann and P. Touborg, Phys. Rev. (To be published). Enclosed.

4) R.J. Elliot, In: Magnetic Properties of Rare Earth Metals. Edited by R.J. Elliot (Plenum, New York, 1972) 1-16.

5) B.R. Cooper, In: Magnetic Properties of Rare Earth Metals. Edited by R.J. Elliot (Plenum, New York, 1972) 17-80.

6) A. Abragam and B. Bleaney, Electron Paramagnetic Resonance of Transition Ions (Clarendon, Oxford, 1970). 665-678.

7) A.J. Freeman, In: Magnetic Properties of Rare Earth Metals. Edited by R.J. Elliot (Plenum, New York, 1972) 245-333.

8) J.M. Dixon, In: Proceedings of the 1. Conference on Crystalline Electric Field Effects in Metals and Alloys. Université de Montreal. June 26-29, 1974. 323-348.

9) A.R. Mackintosh and H. Bjerrum Møller, In: Magnetic Properties of Rare Earth Metals. Edited by R.J. Elliot (Plenum, New York, 1972) 187-244.

10) W.C. Koehler, In: Magnetic Properties in Rare Earth Metals. Edited by R.J. Elliot (Plenum, New York, 1972) 81-128.

11) W. Marshall and S.W. Lovesey: Theory of Thermal Neutron Scattering (Clarendon, Oxford, 1971) 1-16.

12) ibid., 64-104.

13) ibid., 105-126.

14) ibid., 127-172.

15) K.A. McEwen and P. Touborg, J. Phys. **F3** (1973) 1903-1909.

16) N. Wakabayashi, S.K. Sinha and F.H. Spedding, Phys. Rev. **B4** (1971) 2398-2406.

17) S.K. Sinha, T.O. Brun, L.D. Muhlestein and J. Sakurai, Phys. Rev. **B1** (1970) 2430-2441.

18) For Lu, the phonon energies of Tb were used: J.C.G. Houmann and R.M. Nicklow, Phys. Rev. $\underline{B1}$ (1970) 3943-3952.

19) G.H. Lander, T.O. Brun, J.P. Desclaux and A.J. Freeman, Phys. Rev. $\underline{B8}$, (1973) 3237-3240.

20) J. Høg and P. Touborg, Phys. Rev. $\underline{B9}$ (1974) 2920-2928.

21) J. Høg and P. Touborg, Phys. Rev. $\underline{B11}$ (1975) 520-529.

22) P. Touborg and J. Høg, Phys. Rev. $\underline{B11}$ (1975) 2660-2667.

23) J. Høg and P. Touborg, Phys. Rev. B (to be published).

24) O.W. Dietrich and J. Als-Nielsen, J. Phys. $\underline{C4}$ (1971) 71-79.

25) O. Rathmann and J. Als-Nielsen, Phys. Rev. $\underline{B9}$ (1974) 3921-3926.

26) O.W. Dietrich and J. Als-Nielsen, Phys. Rev. $\underline{153}$ (1967) 711-717.

27) B.V.B. Sarkissian and B.R. Coles, Commun. on Physics (to be published).

28) O. Danielsen and P.-A. Lindgård: Quantum Mechanical Operator Equivalents Used in the Theory of Magnetism. Risø Report No. 259 (1972) 93 pp.

29) H. Bjerrum Møller and M. Nielsen, In: Instrumentation for Neutron Inelastic Scattering Research. Proceedings of a panel held in Vienna, 1-5 December 1969. (IAEA, Vienna, 1970, 49-70).

30) S.M. Shapiro and N. Chesser, Nucl. Instrum. Methods $\underline{101}$ (1972) 183-186.

APPENDIX I

Linearized Least Squares Fit

The least squares fit (LS-fit) is a very convenient method
of analyzing experimental data when these are functions of some
independent variable, e.g. neutron counts as function of energy
transfer in a neutron scattering experiment. The data points are
denoted:

$$
\begin{cases}
\text{Independent variable } X_i \\
\text{Dependent (measured) variable } Y_i \\
\text{having an estimated uncertainty } \sigma_i
\end{cases}
\qquad (A1.1)
$$

Here the measured values Y_i are assumed to be uncorrelated.

The idea is to fit the experimental data with a suitable
function $F(X;\underline{P})$, depending on a number (M) of parameters $(P_1, P_2$
.... $P_M) = \underline{P}$. Usually these parameters describe the properties
to be extracted from the experimental data. The overall error of
the fit is given in terms of a weighted sum

$$
\chi^2 = \sum_i (Y_i - f(X_i; \underline{P}))^2 \, W_i. \qquad (A1.2)
$$

The statistically best fit is given by the parameters $\underline{P}$ for
which χ^2 takes its absolute minimum, and with weights given by

$$
W_i = \sigma_i^{-2}. \qquad (A1.3)
$$

To ensure that $\chi^2 = \chi^2 (\underline{P})$ takes a minimum value, we require the
derivatives to be zero

$$
\frac{\partial}{\partial P_k} \chi^2 = 0, \quad k = 1, 2 .... N. \qquad (A1.4)
$$

Unfortunately, this equation only ensures a local minimum
or maximum. Other (physical or mathematical) arguments must be
used to prove it to be an absolute minimum.

For fitting functions $F(X;\underline{P})$ linear in the parameters $\underline{P}$,
these may be found directly, but in general an iterative method

must be used, and, most practically, on a digital computer. For a "guessed" parameter set $\underline{P}^{(n)}$, not too far from the optimal values, one may calculate corrections $\Delta\underline{P}$ to $\underline{P}^{(n)}$ by linearizing $F(X; \underline{P})$ with respect to $\underline{P}$. By inserting into eq. (A1.4) we find

$$\Delta\underline{P} = \underline{A}^{-1} \underline{G} \tag{A1.5}$$

where the symmetric matrix $\underline{A}$ is given by

$$A_{jk} = \sum_{i=1}^{N} W_i \left[\frac{\partial}{\partial P_j} F(X_i; \underline{P}^{(n)}) \right] \left[\frac{\partial}{\partial P_k} F(X_i; \underline{P}^{(n)}) \right] \tag{A1.6}$$

and the gradient vector $\underline{G}$ by

$$G_k = -\frac{1}{2} \frac{\partial}{\partial P_k} \chi^2 = \sum_{i=1}^{N} W_i (Y_i - F(X_i; \underline{P}^{(n)})) \cdot \frac{\partial}{\partial P_k} F(X_i; \underline{P}^{(n)}). \tag{A1.7}$$

Now, $\underline{P}^{(n+1)} = \underline{P}^{(n)} + \Delta\underline{P}$ is expected to be a better set of parameters that may be used as a basis for the calculations A1.5-A1.7 in a new iteration cycle (n+1). In the normal iteration, χ^2 and the ΔP_k's become smaller and smaller as the minimum of χ^2 is approached (convergence). The iteration is stopped when the ΔP_k's become sufficiently small, that is small compared to the statistical uncertainties $\sigma(P_k)$ which will be explained below or to the P_k's themselves. The weakness in the method is obviously that one has to guess the first set of parameters to start the iteration, and these parameters must be in the neighbourhood of the minimum of χ^2. If the guess parameters are too far off, the iteration may diverge, that is χ^2 gets larger and larger. In the LS-fit computer program used in this study, the algorithm described above was modified to reduce the tendency to diverge. According to the algorithm by D.W. Marquard, the parameter corrections (A1.5) were modified

$$\Delta\underline{P} = (\underline{A} + \underline{1}\lambda)^{-1} \underline{G}. \tag{A1.8}$$

Here λ is a positive number which in the case of good convergence is kept negligibly small. However, as soon as tendencies to diverge appear (χ^2 is increased), the program will successively

increase λ towards 1. This has the effect of forcing ΔP towards the direction of the steepest decline of χ^2, given by the gradient $G = - 1/2 \underline{grad} \chi^2$.

When an iteration has successfully converged, the goodness of the fit may be judged from the value of χ^2 obtained. If the chosen weights were realistic and if the fitting function F(X;P) was physical, describing the measurements correctly, we expect $\chi^2 \approx 1$. In this case the uncertainty of the obtained parameters is approximately given by the matrix of covariance

$$\underline{C} = \frac{\chi^2}{N-M} \underline{A}^{-1}, \quad C_{kj} = \text{cov.} \{P_k, P_j\} . \qquad (A1.9)$$

So, for example, the standard error is $\sigma\{P_k\} = \sqrt{C_{kk}}$.

The derivation of (A1.9) is rather similar to that of the standard error of a mean value.

One of the limitations of the least squares fitting is the influence of non-statistical errors. Besides systematic instrumental errors, this kind of error may originate from experimental data that contain more details than can be accounted for by the model function F(X;$\underline{P}$). This may cause "statistically best fits" which are physically poor. For example, in certain cases in the present study it was necessary to increase the weights of the most important experimental data in order to get good physical fits.

APPENDIX II

Matrix Elements of Stevens Operators

The Stevens operators O_{LM} are closely related to the so-called Racah operators O_{LM}. These operators are the angular-momentum equivalents to the spherical harmonics and transform like these. The reason for introducing Racah operators is that the matrix elements of these may be expressed in a more convenient form than is the case for the matrix elements of the Stevens operators.

Following Danielsen and Lindegård[28], the connection between the Stevens and the Racah operators may be expressed as

$$O_{LM} = \frac{1}{K_{LM}} \sqrt{\frac{2L+1}{4\pi}} \begin{cases} \frac{1}{2}(O_{L-M} + (-1)^M O_{LM}), & M>0 \\ O_{L0} & M=0 \end{cases}$$

Some of the normalization coefficients, which make the Stevens operators have integral coefficients, are given in table A2.1.

The matrix elements of the Racah operators may be expressed by the 3-J symbols

$$\langle J\, m_1 | O_{LM} | J\, m_2 \rangle = (-1)^{J-m_1} \frac{1}{2^L} \cdot \frac{(2J+L+1)!}{(2J-L)} \begin{pmatrix} J & L & J \\ -m_1 & M & m_2 \end{pmatrix}. \quad (A.2.2)$$

The 3-J symbol, which is only non-zero for $M+m_2-m_1 = 0$ and if J,L and J fulfil the triangle inequalities, is expressed as the complicated sum

$$\begin{pmatrix} j_1 & j_2 & j_3 \\ m_1 & m_2 & m_3 \end{pmatrix} = (-1)^{j_1-j_2-m_3}$$

$$\sqrt{\frac{(j_1+j_2-j_3)!(j_1-j_2+j_3)!(-j_1+j_2+j_3)!(j_1+m_1)!(j_1-m_1)!(j_2+m_2)!(j_2-m_2)!(j_3+m_3)!(j_3-m_3)!}{(j_1+j_2+j_3+1)!}}$$

$$\cdot \sum \frac{(-1)^k}{k!(j_1+j_2-j_3-k)!(j_1-m_1-k)!(j_2+m_2-k)!(j_3-j_2+m_1+k)!(j_3-j_1-m_2+k)!}$$

Table A2.1

Coefficients connecting Racah and Stevens operators. From [28].

L	M	$\dfrac{1}{K_{LM}}\sqrt{\dfrac{2L+1}{4\pi}}$	L	M	$\dfrac{1}{K_{LM}}\sqrt{\dfrac{2L+1}{4\pi}}$
2	0	2	6	0	16
2	2	$\dfrac{2}{\sqrt{3}}$	6	2	$\dfrac{32}{\sqrt{210}}$
4	0	8	6	3	$\dfrac{16}{\sqrt{210}}$
4	2	$\dfrac{4}{\sqrt{5}}$	6	4	$\dfrac{16}{3\sqrt{7}}$
4	3	$\dfrac{4}{\sqrt{70}}$	6	6	$\dfrac{32}{\sqrt{462}}$
4	4	$\dfrac{8}{\sqrt{35}}$			

APPENDIX III

Resolution of the TAS

The finite resolution of the triple-axis spectrometer derives from the monochromotor and analyzer systems that define the incident and scattered wavevectors $\underline{k}$ and $\underline{k}'$ unsharply.

Although the vertical resolution is quite large it is disregarded here because the vertical components (perpendicular to the scattering plane) of $\underline{k}$ and $\underline{k}'$ have a minor influence on the energy transfer.

Because the monochromator and analyze~ systems are quite similar, we shall only consider the monochromator system set for the (mean) wavevector $\underline{k}_o$. The two independent sources of the $\underline{k}$ unsharpness are indicated in fig. A3.1: finite collimations and mosaic spread. The collimators, consisting of parallel Cd-coated steel plates, may be characterized by their horizontal angular
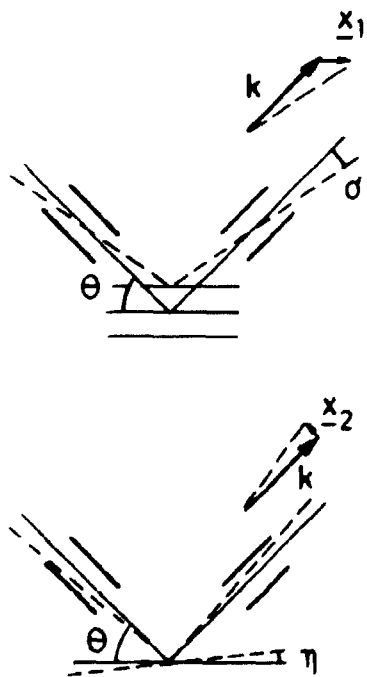

Fig. A3.1 Wavevector spread of monochromator (or analyzer). The two independent sources are indicated:
(1) Upper part: The divergence of the collimators (in com- nation: σ) produces a spread $\underline{X}_1$ (FWHM).
(2) Lower part: The mosaic spread (of the crystal orientation throughout the monochchroma- tor crystal) produces a spread $\underline{X}_2$ (FWHM).

divergences σ_1 and σ_2, i.e. (plate distance)/(collimator length).
The probability for a neutron to pass through a collimator is
approximately a Gaussian function of the angular deviation of the
neutron path from the collimator direction. The mosaic spread,
the slight variation in orientation of the reflecting plane when
going from one mosaic block of the monochromator crystal to
another, is also approximately Gaussian-distributed with an angular
width η (FWHM).

The wavevector deviations X_1 and X_2, indicated in fig. A3.1,
correspond to a FWHM of the unsharpness introduced by finite col-
limation and mosaic spread, respectively, and they are connected
to σ_1, σ_2 and η by [29]:

$$\left\{ \begin{array}{l} X_{1\,E} = 2\,E\,\cot\theta \left[\dfrac{\sigma_1^2\,\sigma_2^2}{\sigma_1^2+\sigma_2^2}\right]^{1/2} \\[2em] X_{1\varkappa} = \dfrac{k_1}{\sin\theta}\left[\dfrac{\sigma_1^2\,\sigma_2^2}{\sigma_1^2+\sigma_2^2}\right]^{1/2} \\[2em] U_1 = \theta \end{array} \right. \tag{A3.1}$$

$$\left\{ \begin{array}{l} X_{2E} = 2\,E\,\cot\theta\left[\dfrac{\sigma_2^2-\sigma_1^2}{\sigma_2^2+\sigma_1^2}\cdot\dfrac{4}{\sigma_1^2+\sigma_2^2}+\dfrac{1}{\eta^2}\right]^{-1/2} \\[2em] X_{2\varkappa} = \dfrac{k_1}{\sin U_2}\,\dfrac{2\sigma_2^2}{\sigma_1^2+\sigma_2^2}\left[\dfrac{4}{\sigma_1^2+\sigma_2^2}+\dfrac{1}{\eta^2}\right]^{-1/2} \\[2em] \tan U_2 = \tan\theta\,\dfrac{2\sigma_2^2}{\sigma_2^2-\sigma_1^2}\,,\qquad 0 \le U_2 < 180^{\circ} \end{array} \right. \tag{A3.2}$$

Here the subscripts "$\varkappa$" and "E" indicate the "normal" wave-
vector diviation $\underline{X} = \underline{k} - \underline{k}_o$ and the corresponding energy deviation,
respectively. U is the angle between $\underline{X}$ and $\underline{k}_o$, while θ is the
Bragg angle.

The total probability for passing through the monochromator
is thus approximately

$$F_M(\underline{\Delta}) = \exp \left\{ - \left(\frac{\Delta_1}{X_1}\ 2\sqrt{\ln 2}\right)^2 - \left(\frac{\Delta_2}{X_2}\ 2\ \sqrt{\ln 2}\right)^2 \right\},\qquad \textbf{(A3.3)}$$

where Δ_1 and Δ_2 are the components of $\underline{\Delta} = \underline{k} - \underline{k}_o$ along $\underline{X}_1$ and $\underline{X}_2$ with $\underline{\Delta}_1 + \underline{\Delta}_2 = \underline{\Delta}$.

In the same way one finds the resolutional widths $\underline{X}_3$ and $\underline{X}_4$ for the analyzer system.

In all, the observed intensity for the setting $(\underline{\varkappa}_o,\ \omega_o)$ may be written in terms of a total resolution function

$$I(\underline{\varkappa}_o,\ \omega_o) = \iint R(\underline{\varkappa} - \underline{\varkappa}_o,\ \omega - \omega_o)\frac{d^2\sigma}{d\Omega dE'}(\underline{\varkappa}',\ \omega')\ d\varkappa' d\omega'. \qquad \text{(A3.4)}$$

The derivation of the total resolution function $R(\underline{\varkappa} - \underline{\varkappa}_o,\ \omega - \omega_o)$ from the monochromator and analyzer distributions, $F_M(\underline{k} - \underline{k}_o)$ and $F_A(\underline{k}' - \underline{k}'_o)$, is not given here. It will depend on the spectrometer setting $(\underline{\varkappa}_o,\ \omega_o)$, including reflectivity factors $R_M(k)$ and $R_A(k')$ for the monochromator and analyzer crystals respectively, and a counter efficiency factor $E(k')$. Fortunately, as the four sources of resolution are independent, one may find the resolutional width in some scan by finding the four contributions separately and adding them quadratically

$$W = \left(\sum_{i=1}^{4} W_i^2\right)^{1/2} \qquad \text{(A3.5)}$$

Effect on Bragg reflection

The scattering from a Bragg reflection with wavevector transfer $\underline{\tau}$ directly gives, apart from a multiplicative factor, the resolution function for the setting $(\underline{\varkappa} = \underline{\tau},\ \omega = 0)$. This appears from the Bragg cross section

$$\frac{d^2}{d\Omega\ dE'}\Big)_B\ \propto\ \delta(\underline{\varkappa} - \underline{\tau})\ \delta(\omega),$$

so that the measured intensity from eq. (A3.4) is

$$I(\underline{\varkappa}_o,\ \omega_o) \propto \iint R(\underline{\varkappa} - \underline{\varkappa}_o,\ \omega - \omega_o)\ \delta(\underline{\varkappa} - \underline{\tau})\ \delta(\omega)\ d\varkappa d\omega \qquad \text{(A3.6)}$$

$$= R_{\underline{\tau},o}(\underline{\tau} - \underline{\varkappa}_o,\ -\omega_o)$$

Effect on inelastic scattering without dispersion

When observing inelastic scattering from excitations (e.g. magnetic or elastic), one must generally take into account the correlation between κ and ω in the resolution function. However, when dispersion-free excitations are dealt with

$$\frac{d^2}{d\kappa\, dE'} \propto f(\kappa)\ \delta(\omega - \omega_0),$$

one may clearly disregard the κ-part of the resolution function. In this simple case we get the energy resolution

$$W_E = (\sum_i X_{Ei}^2)^{1/2}. \tag{A3.7}$$

Examples of this sort of scattering are inelastic scattering from CEF-excitations and the elastic incoherent scattering from V. Equation (A3.7) was used to calculate the energy resolutions presented in fig. 3.3.

Integrated Intensity of Energy Scan

The integrated intensity

$$\mathcal{L} = \int I(\underline{\kappa}, \omega)\ d\omega$$

of a constant κ energy scan may be expressed in terms of a simple sensitivity function $S(\omega)$[29]. The condition is that the κ-dependence of the intensity of the underlying δ-function-like scattering cross section

$$\frac{d^2\sigma}{d\kappa\, dE'} = a(\kappa)\ \frac{k'}{k}\ \delta(\hbar\omega - \hbar\omega_0(\kappa))$$

is negligible within the area of the resolution function. The expression is

$$\mathcal{L} = a(\kappa)\ \frac{k'}{k} \cdot R_M(k)\ A_M(k)\ R_A(k')\ A_A(k')\ E(k')\ \Phi(k). \tag{A3.8}$$

Here $A_M(k)$ and $A_A(k')$ are the areas of the "resolution ellipses"

$$A_M(k) = \frac{\pi}{4} X_{1\mu} X_{2\mu} \sin(U_1-U_2) \ , \quad A_A(k') = \frac{\pi}{4} X_{3\mu} X_{4\mu} |\sin(U_3-U_4)|$$

and ϕ is the neutron flux per energy unit in the reactor beam.

In the analyzer scans only $F_A(k')$, $A_A(k')$ and $E(k')$ vary with μ, so that the sensitivity factor is

$$S(\mu) \propto k' \ R_A(k') \ A_A(k') \ E(k') \propto \frac{(k')^3}{\tan\theta_A} \ R_A(k') \ E(k') .$$

For the most important spectrometer set-up in this study, this equation was used to calculate the sensitivity, normalized to 1 at $\mu = 0$, as shown in fig. 3.2. The analyzer reflectivity $R_A(k')$ was taken from[30] (see fig. A3.2) and the counter efficiency $E(k')$ was calculated as shown below

$$E(k') = 1 - \exp(- \ n_0 \ 1 \ \sigma_{c, \ 25.3 \ meV} \sqrt{\frac{25.3 \ meV}{E'}})$$

$\sigma_{c, \ 25.3 \ meV} = 5376 \cdot 10^{-24} \ cm^2$ is the capture cross section of the He counter gas at 25.3 meV neutron energy

$n_0 = 5.36 \cdot 10^{19} \ cm^{-3}$ is the density of the atoms at 2 atm.
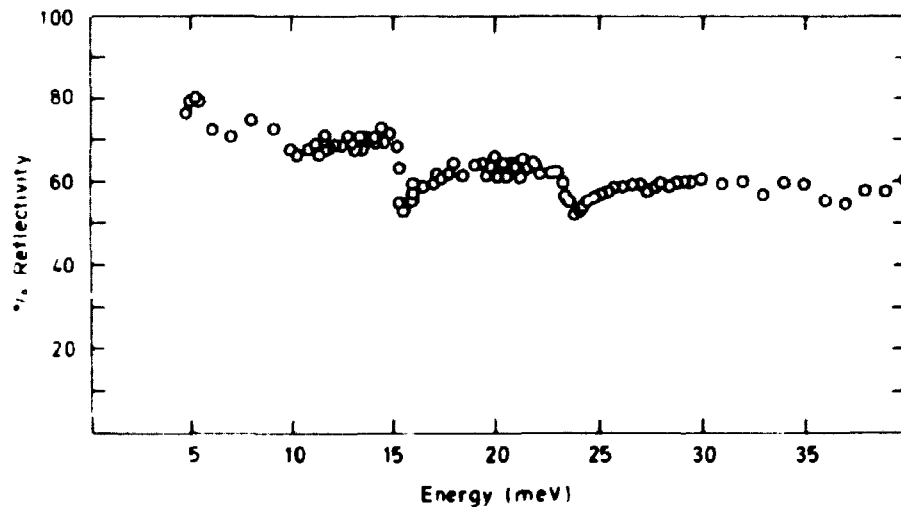
and $1 = 5$ cm is the counter "length".

Fig. A3.2. Reflectivity of pyrolitic graphite[30]. The abscissa is the energy $E = \frac{\hbar^2}{2m} k^2$ of the Bragg-reflected neutron.

APPENDIX IV

Crystal fields in $Er_{0.02}Y_{0.98}$ studied by neutron scattering

O. Rathmann, J. Als-Nielsen, and P. Bak

Atomic Energy Commission Research Establishment Risø 4000 Roskilde, Denmark

J. Høg and P. Touborg

Department of Electrophysics, Technical University, 2800 Lyngby, Denmark

(Received 22 April 1974)

The splitting of the $J = 15/2$ multiplet of Er in an hcp crystal field has been determined by inelastic neutron scattering from a single crystal of $Er_{0.02}Y_{0.98}$. Least-squares fits to the spectra gave crystal-field parameters $B_{20} = -0.34 \pm 0.04$, $B_{40} = (0.7 \pm 0.2) \times 10^{-3}$, $B_{60} = (0.21 \pm 0.02) \times 10^{-5}$, and $B_{66} = (-0.30 \pm 0.03) \times 10^{-5}$ in K, in good agreement with results from bulk magnetization data. A significant line broadening of 1.0 meV full width at half-maximum was clearly observed in the first excited state at 2.2 meV.

INTRODUCTION

The dominant interactions which determine the magnetism of rare-earth metals and their alloys[1] are the indirect exchange interaction and the crystalline field. In addition, the coupling between the magnetic ions and the lattice often plays an important role. In order to separate out the crystal-field interaction for a systematic study Touborg and Høg[2] have investigated a number of rare-earth ions diluted in the nonmagnetic metals Y, Lu, and Sc, which all have the hcp structure of the magnetic heavy rare earths. From magnetization measurements they deduced the parameters B_{lm} in the single-ion crystal-field Hamiltonian

$$H_{cf} = B_{20}\hat{O}_{20} + B_{40}\hat{O}_{40} + B_{60}\hat{O}_{60} + B_{66}\hat{O}_{66} , \qquad (1)$$

where $\hat{O}_{lm}$ are the usual Stevens operators.[3] They found that the point-charge model is totally inapplicable for calculating the crystal fields in the rare-earth metals. This result, perhaps not surprising in itself, contrasts sharply with the conclusions of systematic inelastic-neutron-scattering studies of the rare-earth pnictides[4] and Al_2 compounds,[5] from which it was deduced that an effective-point-charge model can account quite well for the crystal-field levels in these metallic or semimetallic compounds. Since the results on the dilute rare-earth alloys seem to have considerable significance for our understanding of the origin of crystal fields in metals, we decided to investigate the reliability of the crystal-field parameters derived from the magnetization data by using the direct spectroscopic method of neutron scattering. The results which we present here for a single crystal of 2% Er substitutionally disolved in Y are, to our knowledge, the first which have been obtained by neutron scattering on the crystal-field levels of a dilute alloy.

EXPERIMENTAL RESULTS

A single crystal of 22 g was prepared as described in Ref. 6. The intensity spectrum of scattered neutrons versus the energy transfer $\hbar\omega = E - E'$ obtained on a triple-axis spectrometer with a fixed filtered energy E of 14.4 meV and a constant wave-vector transfer $\vec{\kappa} = \vec{k} - \vec{k}'$ is shown in Fig. 1, top and middle part. In the top part the wave-vector transfer was 1.8 Å⁻¹ along the b axis and in the middle part it was 1.8 Å⁻¹ along the c axis in the hcp structure. The sample temperature was 5 K, so only elastic scattering or scattering from the crystal-field ground level with energy loss could occur. The neutron spectra contained four well-defined peaks. The small statistical errors of the two peaks at 3.8 and 5.1 meV were obtained by repeating this part of the spectrum six times.

The relatively low background level is quite remarkable considering the fact that the concentration of the magnetic ions is only 2%.

The peak around $\hbar\omega = 0$ for $\vec{\kappa}$ along the c axis (ΓA) is predominantly due to nuclear incoherent scattering. For κ along the b axis (ΓM) this elastic peak has increased by 75% due to magnetic transitions within the ground-state level.

From the scattering cross section [Eq. (3a)] to be discussed shortly, it can be seen that the elastic magnetic intensity varies as $\cos^2\zeta$, where ζ is the angle between κ and the hexagonal plane. Figure 2 shows the experimental variation with κ and it is concluded that variations in the intensity due to geometrical effects such as those arising from finite sample size in a inhomogeneous beam are small. The peaks at 2, 3.8, and 5.1 meV are due to crystal-field transitions from the ground state to the excited states. We measured the peak around 2.1 meV for κ out to 3.2 Å⁻¹ along ΓM. The intensity varied approximately as the squared
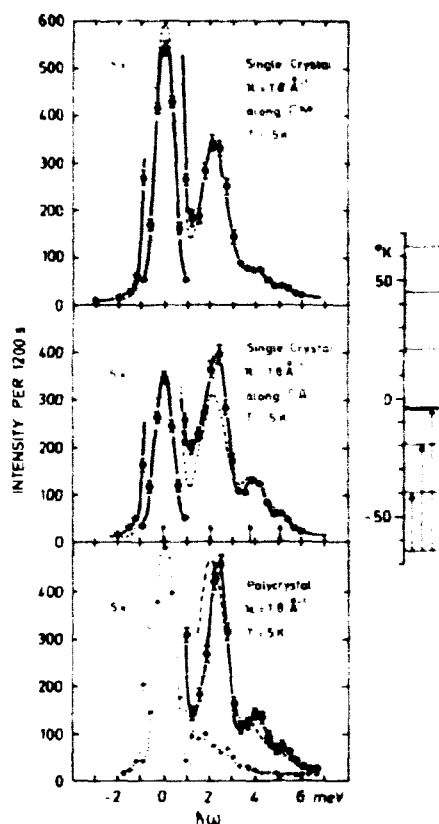
FIG. 1. Inelastic neutron spectra at wave-vector trans-
fer $\vec{\tau} = 1.8$ Å^{-1}. The upper and middle parts are from a
single crystal with $\vec{\tau}$ along the b axis and c axis, respec-
tively, while the bottom part derives from a polycrystal-
line sample. The full line is a guide to the eye of the
$Er_{0.02}Y_{0.98}$ data. The statistical errors are indicated by
error bars where they exceed the size of the circles.
In the bottom part, in addition, the scattering from a
pure Y polycrystal is shown by crosses with a dotted
guide-to-the-eye line. The dashed line is the best simul-
taneous fit to both single-crystal spectra obtained by
diagonalizing Eq. (1) and using a common intrinsic line-
width for all transitions to excited levels. The correc-
tion for instrumental resolution effects has been included
in this fit.

form factor,[7] demonstrating unambiguously that
the scattering is magnetic.

The spectra were also measured at 20 and 50 K.
The intensities of all transitions seen at 5 K were
observed to decrease due to depopulation of the
ground-state level. At the same time a peak at
2.1 meV neutron energy gain appeared, originating
from transitions from the now populated first ex-
cited level to the ground state.

Scattering from lattice vibrations do not con-

tribute to the single-crystal spectra. The momen-
tum-energy-conservation laws determining phonon
scattering are not fulfilled anywhere within the
spectra if the dispersion relation for pure Y is
used,[6] and a few observed phonons propagating in
the symmetry directions showed that resonant
modes of vibration due to the heavy impurity Er
ions do not change the phonon spectrum appreciate-
ly from that of pure Y.

In an intermediate stage of its preparation the
$Er_{0.02}Y_{0.98}$ sample appeared as a polycrystal. A
spectrum from this sample, corresponding to
those of the single crystal, is shown in the bottom
part of Fig. 1, and the same transitions from the
ground level to the excited levels can be identified.
For comparison, the scattering from a 25 g pure
Y polycrystal at 5 K is also shown. For the poly-
crystalline material a small phonon contribution
is observed around 1-3 meV.

In order to compare the raw spectra with the
appropriate scattering cross sections, the instru-
mental resolution effects must be considered, and
the correction for these effects will now be dis-
cussed in some detail. With a fixed incident en-
ergy in the triple-axis spectrometer, the resolu-
tion of the analyzer becomes more and more nar-
row with increasing $\hbar\omega$, and the observed intensity
correspondingly lower. It has been shown by two
independent methods[9,10] that the intensity decrease
varies as $k'^3/\tan(\theta_A)$, where θ_A is the Bragg angle
in the analyzer. Furthermore, the reflectivity of
the analyzer crystal, pyrolytic graphite in (002) re-
flection, varies with $\hbar\omega$[11] and the detector efficiency
also varies slightly with $\hbar\omega$. All these factors as
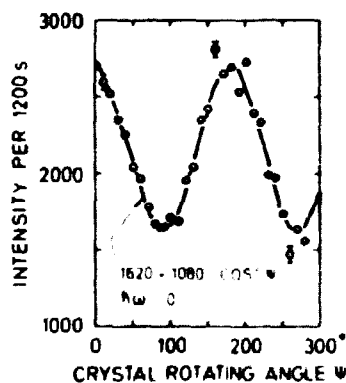well as the factor k'/k, which appears in all in-

FIG. 2. Neutron scattering intensity from the Y pure
single crystal at zero energy transfer and at $\tau = 1.8$ Å^{-1}
measured as a function of the angle between $\vec{\tau}$ and the
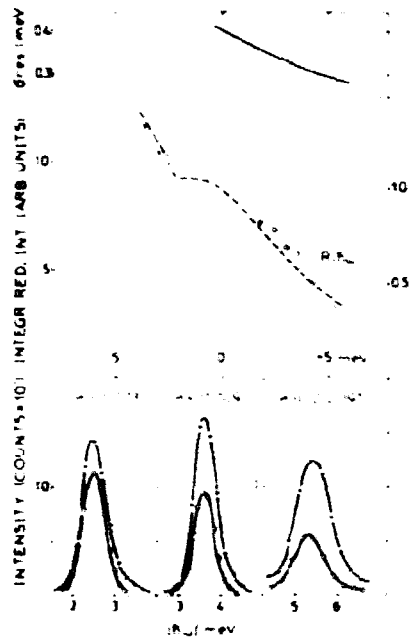hexagonal plane.

Fig. 3. Bottom: Phonon scattering data used to check the instrumental resolution correction. The scattering cross section is given in units of the reciprocal lattice. Crosses denote phonon annihilation, open circles phonon creation. Middle: Integrated reduced phonon intensities (see text) compared to the calculated instrumental resolution correction $R(\hbar\omega)$ (right scale). Top: instrumental resolution width σ_{res}, defined by the resolution function $\exp[-\hbar\omega^2 / 2\sigma_{res}^2]$, vs $\hbar\omega$.

elastic scattering cross sections, are taken into account in a correction factor $R(\hbar\omega)$ normalized to unity at $\hbar\omega = 0$ and shown as the dashed curve in the middle part of Fig. 3. Evidently the variation with $\hbar\omega$ is by no means negligible, so we have checked this variation experimentally by phonon scattering from the same Er$_{0.02}$Y$_{0.98}$ sample at room temperature. In the bottom part of Fig. 3 are shown the phonon scattering from the annihilation and the creation of two TA phonons (left) and one LA phonon (right) all propagating along the c axis. The phonon cross section is in standard notation[12]:

$$\frac{d^2\sigma}{d\Omega\, dE'} \sim \sum_k \frac{k'}{k} A_2^{-1} [\ldots - l_{ph}]\, \delta(\vec{k} - \vec{\tau} - \vec{q}_{ph}) , \qquad (2a)$$

with

$$x_i \sim \mathscr{H}_{c\tau} \frac{k^2 k^2}{2 M F_{ph}} |n_i k_{ph} + \tfrac{1}{2} \pm \tfrac{1}{2}|\, e^{-2\Phi_i m} \qquad (2b)$$

and

$$\sim l_{ph} \sim [\exp E_{ph}/kT - 1]^{-1} , \qquad (2c)$$

In Eq. (2b) the $+$ sign is used for phonon creation, the $-$ sign for annihilation. In the middle part of Fig. 3 are shown the integrated phonon intensities divided by A_2. This quantity is expected to vary as $R(\hbar\omega)$ discussed above, and the agreement in the interval $0 < \hbar\omega < 5$ meV where we apply the resolution correction to the crystal-field spectrum is indeed very good.

ANALYSIS

The $4f$ ground-state multiplet of Er, with $J = \tfrac{15}{2}$, is split by the crystal field into eight doublets. In accordance with the notation of Marshall and Lovesey,[12] we denote the energies by E_n and the states by $|\Gamma_n r\rangle$, with $n = 0$ as the index for the ground state with $E_0 = 0$. The label r distinguishes between the two degenerated wave functions of each level. The cross section for the transition $\Gamma_0 \to \Gamma_n$ is then

$$\frac{d^2\sigma}{d\Omega\, dE'} = c N \frac{k'}{k} A_i T_n \delta(\hbar\omega - E_n) , \qquad (3a)$$

with

$$A_i = \left(\frac{1.91 c^2}{m_e c^2} \frac{1}{2} g\, F(\vec{\kappa})\right)^2 e^{-2W(\kappa)} , \qquad (3b)$$

and

$$T_n = \sum_{\alpha\beta} (\delta_{\alpha\beta} - \hat{\kappa}_\alpha \hat{\kappa}_\beta) \sum_{r r'} P_0 \langle r \Gamma_0 | J_\alpha^* | \Gamma_n r' \rangle$$
$$\times \langle r' \Gamma_n | J_\beta | \Gamma_0 r \rangle \qquad (3c)$$

N is the total number of atoms, the fraction $c = 0.02$ being Er atoms. The g factor is 1.2 for Er and the remaining symbols in Eq. (3b) have their usual meaning.[12] In the expression for the transition probabilities Eq. (3c), $\hat{\kappa}_\alpha$ is the Cartesian α component of $\vec{\kappa}/\kappa$, and P_0 is the occupation probability of one of the two ground states. At 5 K, P_0 is near 0.5.

The spectra in Fig. 1, $I_{c,F}(\hbar\omega)$, were analyzed by a least-squares fit to the expression

$$I_{c,F}(\hbar\omega) = S\left(\sum_n T_n (\sqrt{2\pi}\sigma_n)^{-1} \exp[-(\hbar\omega - E_n)^2 / 2\sigma_n^2]\right)$$
$$+ a_{el} \exp[-(\hbar\omega/\sqrt{2}\sigma_0)^2] + B. \qquad (4)$$

Here the δ function in Eq. (3a) has been changed to a Gaussian distribution of width σ_n in order to take the instrumental resolution as well as an intrinsic linewidth into account. The width σ_0 for elastic scattering is known from a scan of the incoherent scattering from V, whereas the widths for inelastic transitions contained one adjustable parameter σ, in the expression $\sigma_n^2 = (\sigma^2 + \sigma_{res,n}^2)$, with the resolution width $\sigma_{res,n}$ given in the top part of Fig. 3. The factor $R(\hbar\omega)$ accounts

TABLE I. Crystal-field parameters for Er^{3+} in $Er_{0.2}Y_{0.8}$.

	This experiment	From magnetization data
B_2^0 (K)	-0.34 ± 0.04	-0.31 ± 0.03
B_4^0 (K)	$1.7 \times 10^{-2} \times 10^{-2}$	$1.6 \times 10^{-2} \times 10^{-2}$
B_6^0 (K)	$0.21 \pm 0.02 \times 10^{-4}$	$0.24 \pm 0.02 \times 10^{-4}$
B_6^6 (K)	$-0.30 \pm 0.02 \times 10^{-3}$ *	$-0.28 \pm 0.03 \times 10^{-3}$
Γ (meV)	0.53 ± 0.05	

*The sign is undetermined by the neutron scattering experiment.

for the decreasing instrumental sensitivity as explained above. The nuclear incoherent scattering is accounted for by the fit parameter σ_{ni}. The background B was determined by the intensities with $E_a = -3$ meV and $E_b = 7$ meV.

The transition probabilities I_n and the energies E_n are determined by the crystal-field parameters B_2^0, B_4^0, B_6^0, and B_6^6. Finally, the scale factor S was also a fitting parameter. The best-fit value of S agreed with the value obtained from the intensity observed with a Y sample of similar shape to the $Er_{0.2}Y_{0.8}$ sample.

The calculated spectra obtained in a *simultaneous fit to both* spectra in Fig. 1 are shown as dashed lines in Fig. 1, and the resulting best-fit parameters are given in Table I. The dashed line in the bottom part of Fig. 1 is a powder spectrum calculated from this set of parameters. The small phonon contribution is included in this theoretical spectrum.

The corresponding energy levels are shown in the right part of Fig. 1 and the centers of the transition peaks are indicated by arrows on the energy axis.

The ground-state level, from which the strongly anisotropic magnetic elastic scattering originates, turns out mainly to consist of $\pm\frac{13}{2}$ states, while the inelastic peaks in the spectra are due to transitions to three excited levels dominated by $\pm\frac{11}{2}$, $\pm\frac{7}{2}$, and $\pm\frac{15}{2}$, respectively. When $\vec{\kappa}$ is along ΓA the magnetic scattering is caused by matrix elements of J_x and J_y. Hence, the small elastic magnetic scattering, about $\frac{1}{3}$ of the value for $\vec{\kappa}$ along ΓM, is purely due to the small components of other $|J_z\rangle$ states than $\pm\frac{13}{2}$ which are mixed into the ground states via the O_6^6 term of the Hamiltonian in Eq. (1). The transition to the first excited level is nearly isotropic because J_x, J_y, and J_z have matrix elements from the ground level to this level of nearly equal size. The last two transitions in the spectra are caused purely by matrix elements of J_x and J_y. Hence, the intensity ratio between the $\vec{\kappa}$ along-ΓA direction and $\vec{\kappa}$ along-ΓM direction should be exactly 2.

At first sight it may seem surprising that one can

deduce four crystal-field parameters with reasonable accuracy and a common lifetime from the upper and middle spectra in Fig. 1. The reason is that the different combinations of matrix elements for $\vec{\kappa}$ along ΓA and $\vec{\kappa}$ along ΓM constrain the possible values of the crystal-field parameters significantly.

It is obviously necessary to include a finite lifetime of the excited states as the width of the peak at 2.1 meV exceeds the experimental resolution by more than 50%. The intrinsic width, which of course cannot be accounted for by the Hamiltonian in Eq. (1), is very likely caused by the exchange interaction between the Er ions. In a 2% alloy there is a 24% chance that an Er ion among its 12 neighbors has another Er ion. If we may crudely assume an Ising-like nearest-neighbor-only exchange coupling $-gJ_z^{(0)}J_z^{(1)}$, it is straightforward by a perturbation calculation to find the corresponding splitting of the degenerate levels in Fig. 1. With $g \sim 0.02-0.04$ meV from the known spin-wave dispersion in pure Er [13,14] we then find a splitting $0.4-0.9$ meV, i.e., in the same order of magnitude as the observed widths of the inelastic peaks.

CONCLUSION

We conclude that the crystal-field parameters obtained from the magnetization data [2] for Er diluted in Y are, within the uncertainties of the two experiments, in accordance with those obtained by the more direct spectroscopic method of neutron scattering. This agreement supports the reliability of the crystal-field parameters found in the systematic study of rare-earth (RE) ions in different matrices. [2] On the other hand, it is also clear from Fig. 1 that the excited states of the Er ions are probed in more detail by neutron scattering than the simple Hamiltonian in Eq. (1) can account for. First there is a significant line broadening, even at 5 K, of the excited levels, most clearly seen in the intense transition to the first excited state. Second, the difference between the best-fit curve based on Eq. (1) and the observed intensities is substantially larger than can be explained by the experimental uncertainties. It seems likely that the interaction between the $4f$ and the conduction electrons is responsible for these effects, either by the direct interaction [14] or by the indirect exchange coupling to nearby Er ions.

[1] *Magnetic Properties of Rare-Earth Metals*, edited by R. J. Elliott (Plenum, New York, 1972).

[2] J. Høg and P. Touborg, Phys. Rev. B **9**, 2920 (1974); P. Touborg and J. Høg, Phys. Rev. Lett. (to be published).

[3] K. W. H. Stevens, Proc. Phys. Soc. Lond. A **65**, 209 (1952).

[4] R. J. Birgeneau, E. Bucher, J. P. Maita, L. Passell, and K. C. Turberfield, Phys. Rev. B **8**, 5345 (1973); K. C. Turberfield, L. Passell, R. J. Birgeneau, and E. Bucher, Phys. Rev. Lett. **25**, 752 (1970).

[5] H. G. Purwins, E. Walker, B. Barbara, W. F. Rossignol, and P. Bak, J. Phys. C (to be published).

[6] K. A. McEwen and P. Touborg, J. Phys. F **3**, 1903 (1973).

[7] We have used the value of F ($\kappa = 1 \approx Å^{-1}$) 0.9 as mea-
sured for Tb by Lander *et al.* (Phys. Rev. B __, __ (1973)).

[8] S. K. Sinha, T. O. Brun, L. D. Muhlestein, and J. Sakurai, Phys. Rev. B **1**, 2430 (1970).

[9] H. B. Møller and M. Nielsen in *Instrumentation for Neutron Inelastic Scattering Research* (IAEA, Vienna, 1970), pp. 49–70.

[10] N. Chesser and J. D. Axe, Acta Crystallogr. A **29**, 160 (1973).

[11] S. M. Shapiro and N. Chesser, Nucl. Instrum. Methods **101**, 183 (1972).

[12] W. Marshall and S. W. Lovesey, *Theory of Thermal Neutron Scattering* (Clarendon, Oxford, 1971).

[13] R. M. Nicklow, N. Wakabayashi, M. K. Wilkinson, and R. E. Reed, Phys. Rev. Lett. **27**, 334 (1971).

[14] J. Jensen, J. Phys. F **1**, 1065 (1974).

APPENDIX V

Crystal Fields in Dilute Alloys of Rare Earths in Sc, Y and Lu Studied by Neutron Scattering

O. Rathmann

Atomic Energy Commission Research Establishment Risø,
DK-4000 Roskilde, Denmark

and

P. Touborg

Department of Electrophysics
Technical University of Denmark
DK-2800 Lyngby, Denmark, and
Physics Department, University of Odense
DK-5000 Odense, Denmark

Abstract

The crystal field levels in Sc-Er, Lu-Er and Y-Dy have been studied by neutron spectroscopy. The spectra for Sc-Er and Lu-Er are similar to earlier published spectra for Y-Er and in agreement with the level schemes deduced from bulk magnetization measurements. Disagreements between the two types of measurement for Y-Dy suggest a correction for magnetic ordering in the analysis of the magnetization data. The reanalysed magnetization results are fully consistent with the neutron results.

Introduction

A number of publications describing magnetization measure-
ments on dilute alloys of rare earths in Sc, Y and Lu have re-
cently appeared[1-5]. From these measurements, crystal field pa-
rameters B_{lm} have been deduced in the single-ion crystal field
Hamiltonian

$$H_{cf} = B_{20}O_{20} + B_{40}O_{40} + B_{60}O_{60} + B_{66}O_{66} \qquad (1)$$

where O_{lm} are the usual Stevens' operators[6]. The deduced parameters
vary unsystematically with the rare earth solute, and especially
the parameters obtained for alloys with Dy differ significantly
from those for other solutes. For a given rare earth solute a
variation with the host of the quadrupole component (B_{20}) of the
crystal field is observed. Other components show only small vari-
ations with the host.

In the present paper we report inelastic neutron scattering
experiments on Y-Dy, Sc-Er and Lu-Er alloys. These experiments,
together with the earlier published neutron experiment[7] on
Y-2.0 At%Er, provide a check on the variation of crystal field
parameters with both solute and host.

Experimental technique

Single crystals of the alloys Sc-2.0At%Er, Y-3.0At%Dy,
Y-1.1At%Dy and Lu-2.0At%Er were grown using the technique of
annealing arc melted buttons[8]. The chosen shape and size (typi-
cally 3 cm^3) of the samples were determined from considerations
of neutron absorption. Some of the samples consisted of two single
crystals aligned with the same orientation. All samples were stud-
ied by neutron diffraction, to look for possible ordering, and
by inelastic neutron scattering to observe transitions between
crystal field levels. In the latter experiments the intensity
spectrum of scattered neutrons with fixed wave vector transfer (κ)
and fixed incident energy was measured on a triple axis spectro-
meter with a counting time determined by a preset number of beam
monitor counts (BMC). The incident energy was generally 14.4 meV
and a graphite filter was used to remove second-order contamin-
ation. The energy resolution was about 1 meV. In one case a 5 meV

incident energy and a be filter cooled to ?? K were used to obtain
a resolution of 0.3 meV. The measurements were performed at tem-
peratures down to 5 K using a cryostat with Al-windows.

Experimental results

No ordering was observed at temperatures above 5 K in Sc-
2.0At%Er, Y-1.1At%Dy and Y-2.0At%Er. In Y-3.0At%Dy,helical ordering
with the moments lying in the basal plane was observed below 9 K.
The neutron diffraction scan is illustrated in fig. 1. The spiral
angle is 50° per layer. Inelastic scans above the ordering tem-
perature showed no sign of crystal field transitions, probably
due to the large exchange interactions responsible for the ordering.
Also in Lu-2.0At%Er,magnetic satellites were present. The corre-
sponding order existed at least up to 20 K, indicating that the
ordering takes place in small regions of high Er concentraiton.
An estimate from satellite intensities showed that less than 3%
of the Er takes part in the ordering. Thus the ordering may be
neglected in interpreting the inelastic scattering experiment.

The neutron scattering intensity spectrum for Sc-2.0At%Er is
shown in fig. 2a. Two transitions, indicated by arrows, are ob-
served. The transition energies determined by a least squares fit
of a sum of Gaussians to the spectra are shown in fig. 2b. These
results are in agreement with the crystal field parameters deter-
mined from analysis of magnetization measurements[9],as can be seen
by comparison with fig. 2c. At the temperature 6.5 K of the neu-
tron experiment only the crystal field ground level is populated.
Thus only transitions from this level to excited levels are ob-
served. Measurements at higher temperatures or with larger wave
vector transfer give the same spectrum as fig. 2a,but with de-
creased intensities of the transition peaks. This behaviour, also
seen for the other samples, is in agreement with what is expected
for pure crystal field transitions.

The spectra for Lu-2.0At%Er, fig. 3a, show one significant
peak (arrow at lower energy) and contain evidence of another
(arrow at higher energy). Also for Lu-2.0At%Er the transition
energies, fig. 3b, can be successfully compared with the crystal
field level scheme, fig. 3c, obtained from analysis of magnet-
ization measurements[9].

The spectra at 5K for Y-1.1At%Dy show one transition shoulder

(arrow in fig. 4a). The identification of the shoulder as a crystal field transition is supported by the decrease in intensity at 30K also shown in fig. 4a. An attempt to resolve the transition peak completely by using an energy resolution of 0.2 meV was unsuccessful, because it has an inherent width of about 1 meV. The transition energy 1.33±0.2 meV (fig. 4b) is in clear disagreement with the crystal field levels calculated from earlier deduced parameters (fig. 12 in ref. 1). However, the knowledge that ordering effects are present has made it possible to correct the magnetization data for these effects. An analysis of the corrected data gives crystal field parameters which predict the observed crystal field transition (fig. 4c) and no other observable transitions.

Reanalysis of the magnetization measurements

The crystal field parameters B_{20}, B_{40}, B_{60} and B_{66} are determined, together with two exchange parameters γ_{11} and $\gamma_{\perp}$ and the concentration, by fits to the inverse initial susceptibility. The fitting procedure is described in ref. 9. Effects of ordering even in the dilute alloy Y-0.137At%Dy are clearly seen in the measurements of the basal plane anisotropy[4]. The presence of a small ordered region may change the initial susceptibility drastically. However the correct paramagnetic susceptibility can in important cases be obtained from isothermal magnetization curves. For an applied field of sufficient magnitude ($H > H_{min}$) all moments in the crystal will be aligned in the field direction, although acted on by different exchange fields dependent on the local concentration. If the sum of the exchange and the applied fields are within the range for which the pure crystal field susceptibility, χ_{CF}, remains at its initial value, we find the following formulae for the differential susceptibility:

$$M_j = (H + \gamma_j \langle M \rangle) \chi_{CF}$$

$$\langle M \rangle = \frac{1}{N} \sum_{j=1}^{N} M_j$$

$$\frac{1}{\chi} = \frac{dH}{d\langle M \rangle}\bigg|_{H > H_{min}} = \frac{1}{\chi_{CF}} - \langle \gamma \rangle \tag{2}$$

$$\langle \gamma \rangle = \frac{1}{N} \sum_{j=1}^{N} \gamma_j$$

The sums are over sites j, γ_j are site-dependent exchange constants and M_j are the magnetic moments. The only difference of (2) from the formulae for an ideal dilute system is the change of γ to $<\gamma>$. The existence of an extended linear range in the magnetically hard directions may be verified theoretically after the parameters have been deduced. (For Y-Dy χ_{CF} varies less than 2% in the range $0 - 70 \cdot 10^5$ A/M.)

The validity of the above theory can be verified experimentally by the presence, in the magnetization curves, of a linear range following the initial high slope range. This feature is clearly seen in the magnetization curve shown in fig. 5 which illustrates the difference at 4.2 K between χ_{CF} and the earlier published susceptibility χ_H = M/H measured at the constant field H = 1.35 x 10^5 A/M. χ_{CF} equal χ_H for Y-0.137 At%Dy at temperatures above 13 K. For Er alloys χ_{CF} equals χ_H in the whole measuring range.

For all alloys measured, the above procedure applies in the hard direction down to 4 K. In the easy directions at low temperature, the initial field independent range of χ_{CF} is too narrow to allow the above procedure. Fortunately the susceptibilities at low temperatures in the easy directions are rather unimportant in determining the parameters.

For Y-0.137 At%Dy, χ_{CF} has been determined from a number of isothermal magnetization curves, and the earlier published $1/\chi$ curves have been corrected. The corrected curves are shown in fig. 6 with new theoretical fits.

For a further check of the revised crystal field parameters for Y-Dy, they were compared to magnetization measurements at higher fields. Figure 7 shows isofield measurements at $44.2 \cdot 10^5$ A/m for Y-0.137 At%Dy[1] together with theoretical curves. The deviation at low temperatures in the c-direction is expected due to the ordering mentioned earlier. In the c-axis magnetization at 4.2 K the deduced crystal field parameters predict a transition at the field $140 \cdot 10^5$ A/m. In a narrow range of $10 \cdot 10^5$ A/m the magnetization should increase 3 μ_B/atom. This is in excellent agreement with the published high field magnetization measurements on Y-Dy[3].

Ordering effects in the Er alloys are too small to give any corrections to the initial susceptibility. This is consistent

with the agreement between the magnetization and neutron results for these.

Conclusion

The neutron experiments have demonstrated the necessity of corrections for ordering effects in some dilute alloys. The tendency for ordering of the rare earth solutes decreases in the series Tb, Dy, Ho, Sm and Er which have Néel-De Gennes factors $((g-1)^2 J(J+1))$ 10.50, 7.08, 4.50, 4.46 and 2.55, respectively. The present results suggest that for the typical alloy concentrations used, corrections to $1/\chi$ measurements on Tb and perhaps Ho and Sm alloys may be necessary.

The crystal field parameters obtained from the magnetization data, corrected if necessary in the way described, are in accordance with the results of the independent and direct method of neutron scattering, and are also consistent with high-field measurements.

Table I lists the crystal field parameters divided by corresponding Stevens factors for the 4 alloy systems successfully checked by neutron scattering. The variation with host of B_{20}/α is probably due to the varying c/a ratio. The higher-order parameters B_{40}/β, B_{60}/γ and B_{66}/γ are within uncertainty independent in their determination of both the host and the rare earth solute.

Acknowledgements

Table I

Crystal field parameters in K divided by Stevens factors for 4 alloy systems. The crystal field parameter B_{66} equal $-\frac{77}{8} B_{60}$, as observed to within the experimental accuracy[9].

	$\dfrac{B_{20}}{\alpha}$	$\dfrac{B_{40}}{\beta}$	$\dfrac{B_{60}}{\gamma}$
Sc-Er[9]	-29 ± 3	$8.2 \, ^{-2}_{+5}$	18.1 ± 2
Lu-Er[5,10]	-55.7 ± 7	9.6 ± 2	16.1 ± 2
Y-Er[2,10]	-111 ± 13	13.5 ± 6	12.0 ± 3
Y-Dy	-115 ± 12	7.5 ± 3.5	13.1 ± 3

References

1) J. Høg and P. Tourborg, Phys. Rev. B 9, 2920 (1974).

2) P. Touborg and J. Høg, Phys. Rev. Lett. 33, 775 (1974).

3) P. Touborg, J. Høg, G.J. Cock and L.W. Roeland, Phys. Rev. B 10, 2952 (1974).

4) J. Høg and P. Touborg, Phys. Rev. B 11, 520 (1975).

5) P. Touborg and J. Høg, Phys. Rev. B 11, 2660 (1975).

6) Magnetic Properties of Rare-Earth Metals, edited by R.J. Elliot (Plenum, New York, 1972).

7) O. Rathmann, J. Als-Nielsen, P. Bak, J. Høg and P. Touborg, Phys. Rev. B 10, 3983 (1974).

8) K.A. McEven and P. Touborg, J. Phys. F 3, 1903 (1973).

9) J. Høg and P. Touborg, Phys. Rev. B (to be published) (The magnetization data on Sc-Tb and Sc-Dy in this reference have been corrected for magnetic ordering as proposed in the present paper).

10) The parameters given here have been obtained by the fitting procedure described in ref. 9 and differ insignificantly from those published earlier.
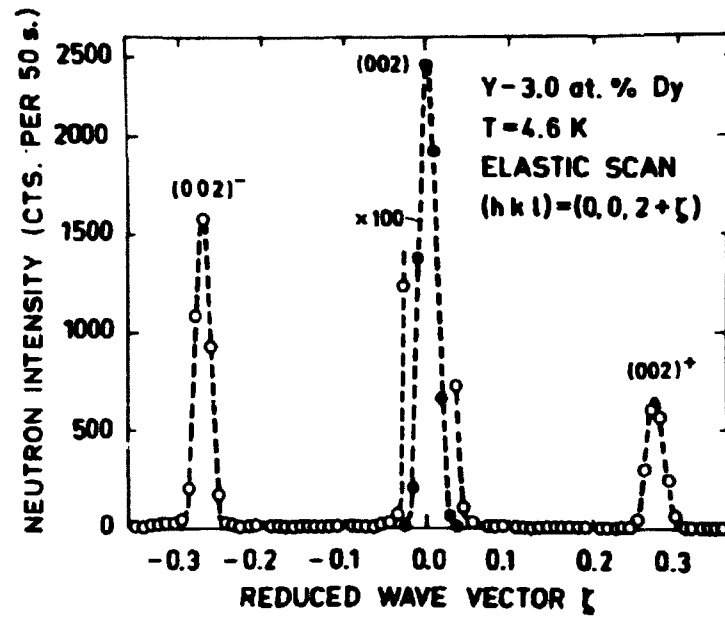
Fig. 1. Neutron diffractions scan for Y-3.0At%Dy along the (002) direction. The satellites (002)$^{\pm}$ are not present above 9 K.
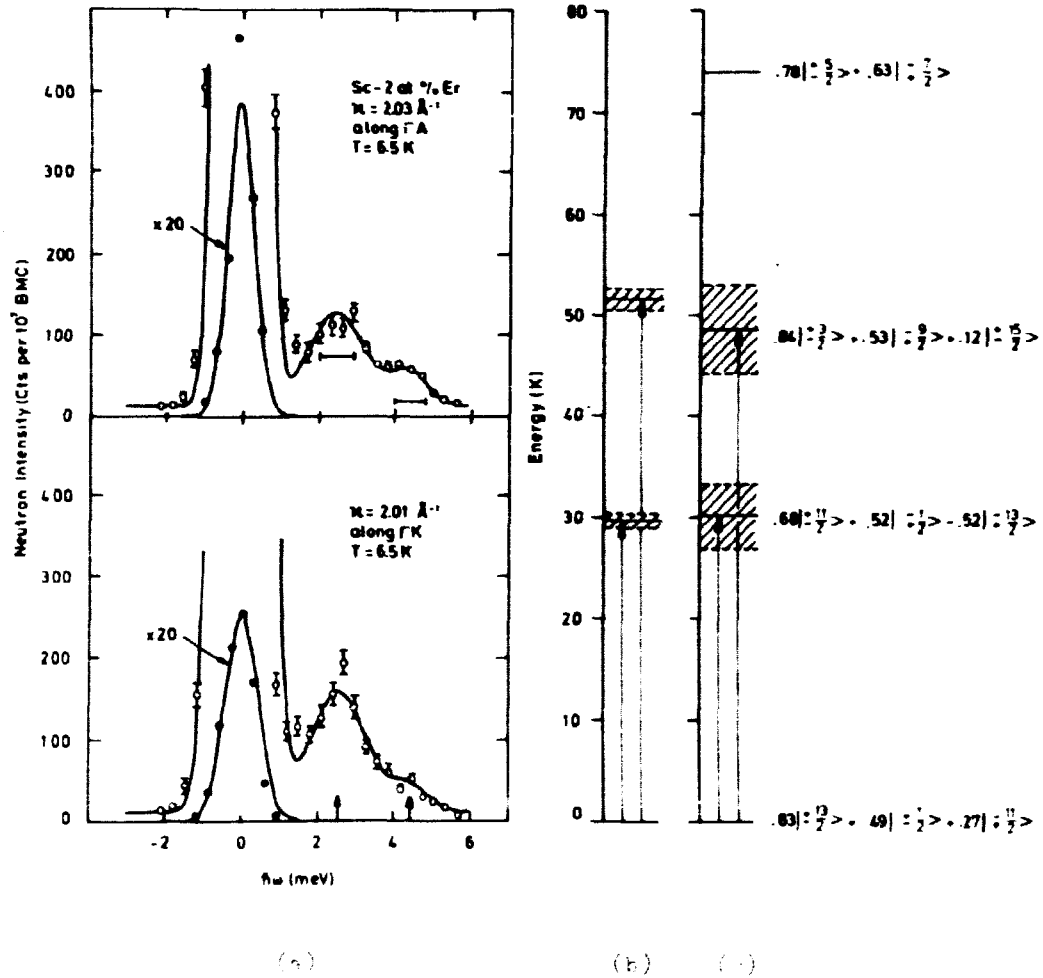
Fig. 2 **a**. Inelastic neutron scattering spectra for Sc-2.0At%Er.
The experimental resolution and statistical uncertainties are
indicated. The full lines are least squares fits. **b**. Transition
energies with uncertainties obtained from the spectra in fig. 2a.
c. Crystal field levels and wave functions calculated from the
following crystal field parameters in K:

$B_{20} = (-7.4\pm0.7)\cdot10^{-2}$, $B_{40} = (3.7^{-0.9}_{+2.2})\cdot10^{-4}$,

$B_{60} = (37.5\pm4.1)\cdot10^{-6}$, $B_{66} = -77/8\cdot B_{60}$.

These parameters have been obtained from an analysis of magnetiz-
ation measurements[8]. The uncertainties in energy of the lowest
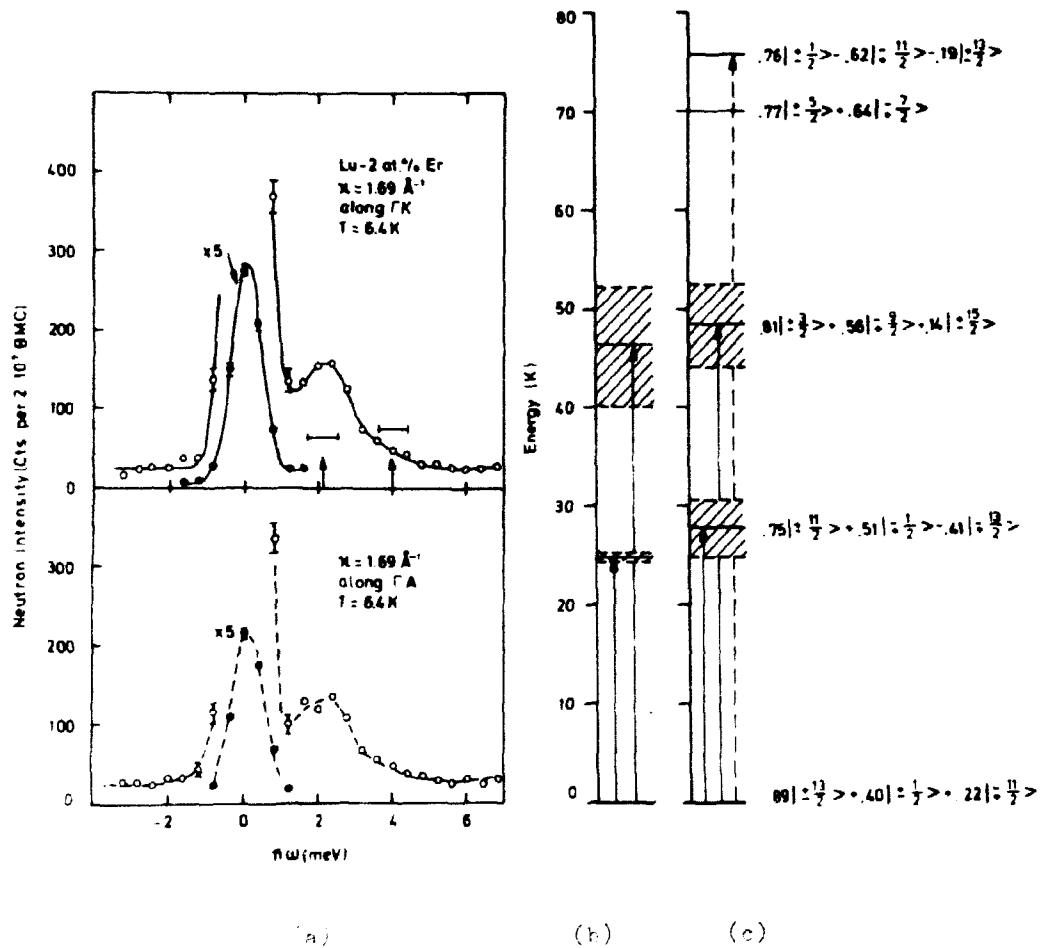levels and observable transitions at zero temperature are indicated.

Fig. 3 a. Inelastic neutron spectra for Lu-2.0At%Er. Resolution and uncertainties are indicated. The full line is a least squares fit. The dashed line is a guide-to-the-eye. b. Transition energies with uncertainties obtained from the spectra in fig. 3a. c. Crystal field levels and wave function calculated from the following crystal field parameters in K:

$B_{20} = -0.141\pm0.018$, $B_{40} = (4.25\pm0.9)\cdot10^{-4}$,

$B_{60} = (33.5\pm4)\cdot10^{-6}$, $B_{66} = -77/8\cdot B_{60}$. These parameters have been obtained from an analysis of magnetization measurements[5,10]. The uncertainties in energy of the lowest levels are indicated. The dashed arrow indicates a possible transition which has too small intensity to be observed experimentally.
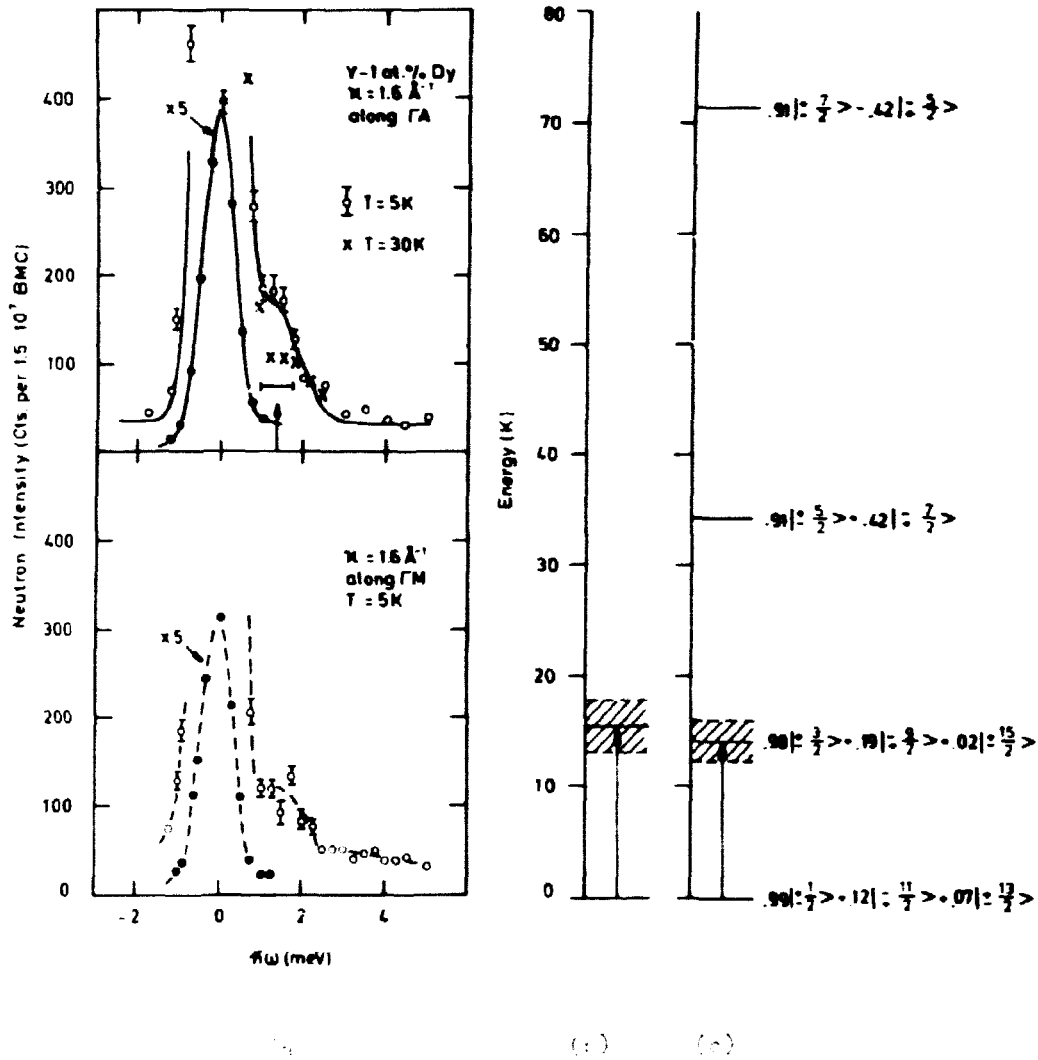
Fig. 4 a. Inelastic neutron spectra for Y-1.1At%Dy. Resolution
and uncertainties are indicated. The full line is a least squares
fit to the spectrum at 5 K. The dashed line is a guide-to-the-eye.
b. Transition energy with uncertainties obtained from the spec-
trum in fig. 4a. c. Crystal field levels and wave function cal-
culated from the following crystal field parameters in K:

$B_{20} = 0.733\pm0.07$, $B_{40} = (-4.5\pm2) \cdot 10^{-4}$,

$B_{60} = (13.5\pm3) \cdot 10^{-6}$, $B_{66} = -77/8 \cdot B_{60}$. These parameters have
been obtained by reanalysis of earlier published magnetization
measurements[1] as described in the text. The uncertainties in
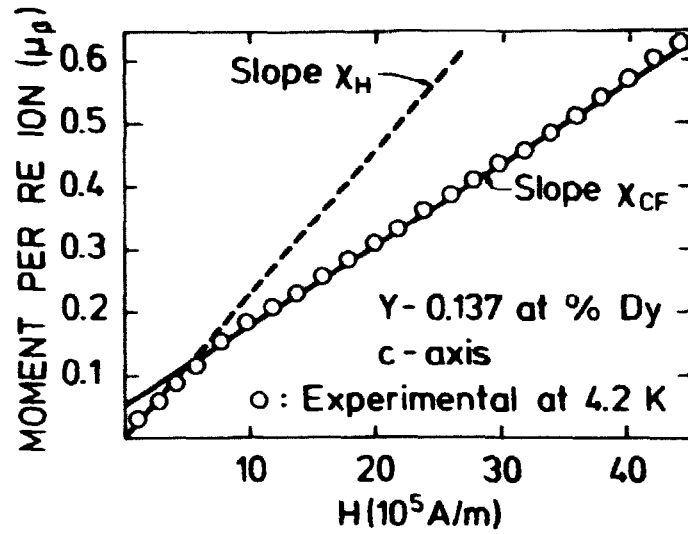energy of the lowest levels are indicated.

Fig. 5. Magnetization at T=4.2K for Y-0.14At%Dy in the c-direction. The experimental differential slope at higher fields, χ_{CF} (slope of full line) and the earlier published susceptibility $\chi_H = \frac{H}{M}$ at $H = 1.35 \cdot 10^5$ A/m (slope of dashed line) are illustrated.
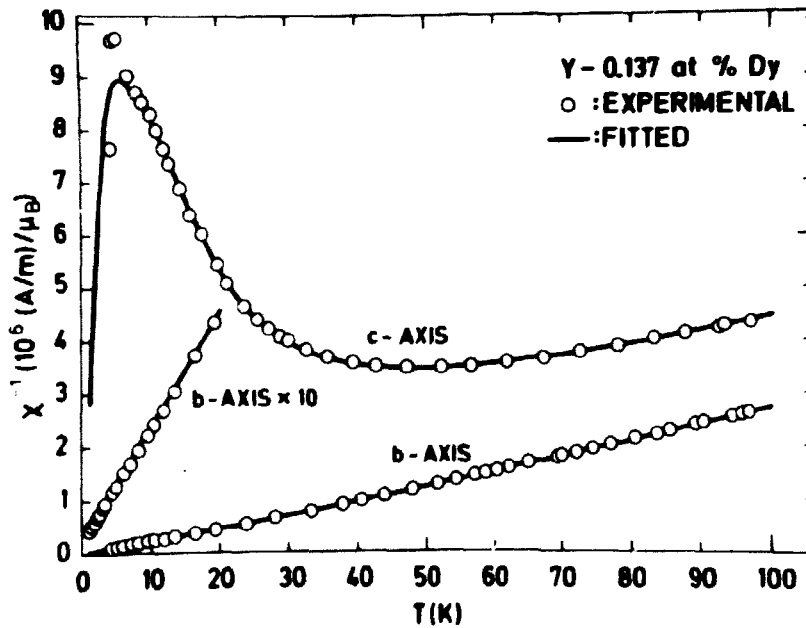

Fig. 6. Reciprocal susceptibility for Y-0.14At%Dy. The experimental points are published data[1] corrected in the c-direction as described in the text. The full curves are theoretical fits, giving the parameters

$B_{20} = (0.733 \pm 0.07)$K, $B_{40} = (-4.5 \pm 2) \cdot 10^{-4}$K,

$B_{60} = (13.5 \pm 3) \cdot 10^{-6}$K, $B_{66} = -77/8 \cdot B_{60}$

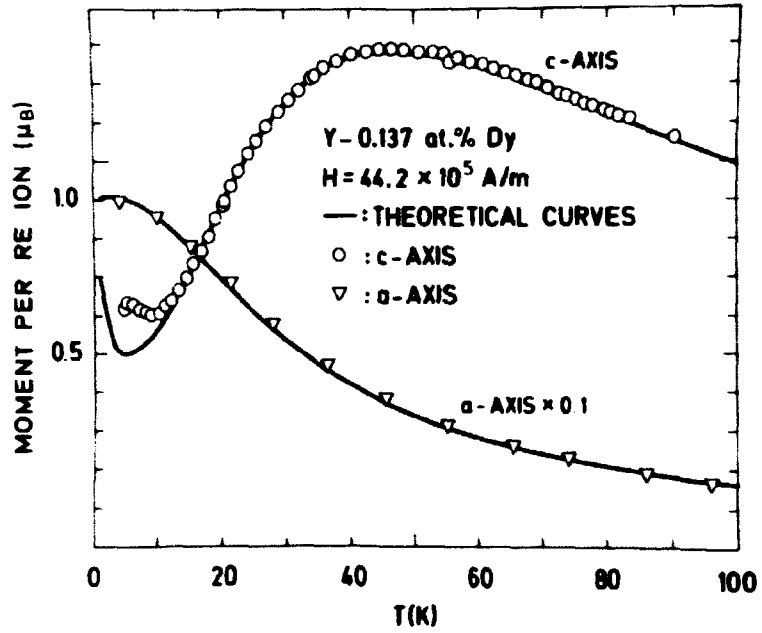$\gamma_{11} = (-0.3 \pm 0.1) \cdot 10^{6}(A/m)/\mu_B$, $\gamma_\perp = 0$

Fig. 7. Isofield curves at 44.5·10⁵ A/m for Y-0.14At%Dy. The experimental points were published earlier[1]. The full curves are calculated using the parameters given in the caption to fig. 6.